AN ABSTRACT OF THE THESIS

Sungkyoo Lim for the degree of Doctor of Philosophy in Electrical and Computer Engineering presented on May 6, 1993. Title: Design, Fabrication, and Testing of Inhomogeneous Dielectrics

Redacted for Privacy

Abstract approved: _____

Dr. John F. Wager

In this thesis the concept of inhomogeneous dielectrics is demonstrated for various optical coating applications. Compositionally-varying silicon oxynitride (SiON) dielectric layers, with the refractive index varying as a function of position, are grown by computer-controlled plasma-enhanced chemical vapor deposition (PECVD) using silane, nitrogen, and nitrous oxide reactant gases. Compositionally graded and superlattice-like SiON layers are grown and their compositional profiles are confirmed by Auger electron spectroscopy sputter profiling. Inhomogeneous antireflection coatings and rugate filters, with sinusoidally varying refractive index profiles, are designed and fabricated and their measured

spectral responses are found to be in excellent agreement with simulated results. Alternating-current thin film electroluminescent (ACTFEL) devices with multiple layer dielectrics also are designed, fabricated, and the insulating layers are shown to increase the optical outcoupling efficiency of an ACTFEL devices by approximately 14 % compared to that of a conventional ACTFEL structure.

Design, Fabrication, and Testing of Inhomogeneous Dielectrics

by

Sungkyoo Lim

A THESIS

submitted to

Oregon State University

in partial fulfillment of
the requirements for the
degree of

Doctor of Philosophy

Completed May 6, 1993

Commencement June 1993

APPROVED:

Redacted for Privacy

Associate Professor of Electrical and Computer Engineering

Redacted for Privacy

Head of Department of Electrical and Computer Engineering

Redacted for Privacy

Dean of Graduate School

Date thesis is presented : May 6, 1993

Typed by Sungkyoo Lim for : Sungkyoo Lim

ACKNOWLEDGMENT

I would like to express my deepest gratitude to my advisor, Prof. John F. Wager, for the idea, support, guidance, and encouragement he has given me throughout this work.

I would also like to thank Professors Curtis R. Cook, Vijai K. Tripathi, Stephen M. Goodnick, and William Hetherington for serving on my committee and sharing their valuable time.

I also wish to thank Planar Systems for supplying glass substrates and growing a phosphor layer for ACTFEL devices and Mr. Luis M. Casas at U.S.Army Electronics Technology and Devices Laboratory, Ft. Monmouth, for doing AES analysis.

Thanks to Dr. Seung-Bae Kim, Wie Ming Ang, Ahmad Abu-Dayah, Tin Nugyeun, and Jae-Hwa Ryu for their assistances and valuable discussions, and Mr. William Hostetler for filing up patents.

The financial support provided by Goldstar is greatly appreciated.

TABLE OF CONTENTS

LIST OF FIGURES

LIST OF TABLES

Design, Fabrication, and Testing of Inhomogeneous Dielectrics

Chapter 1. Introduction

Until recently almost all optical coatings have been designed and fabricated using homogeneous, single or multiple-layer structures[1-5]. The potential advantage of employing inhomogeneous films, whose refractive index varies continuously as a function of position, for optical coating applications has been recognized for a long time since, in principle, they may be used to realize optical thin films with superior spectral properties[6-14]. The primary advantage of inhomogeneous films, compared to conventional multiple layer coatings, is the additional degree of design freedom available because the refractive index can be varied in a continuous fashion. Additionally, the absence of distinct interfaces in an inhomogeneous film suggests that such a coating should be more durable and less chemically sensitive to the environment.

The primary problem with inhomogeneous thin films is that they have been very difficult to fabricate. Even though the growth of inhomogeneous films is very difficult, theoretical analysis of inhomogeneous optical coatings has been undertaken by many authors, and recent

developments of computer technologies have enabled the theorist to calculate the inhomogeneous index profile required for an optical filter[15-24].

It is also possible to control the rates of coating sources by a computer. The codeposition[12,13] and ion assisted deposition(IAD)[14] methods have been the standard techniques used to grow inhomogeneous dielectric layers by controlling the deposition time and other parameters of each source. It is not easy to control the conditions for these compositional deposition methods. It is also difficult to achieve thickness and compositional uniformity using these deposition methods. These problems make it very difficult to apply the above-mentioned methods to mass production.

The principal purpose of the research presented in this thesis is to demonstrate, for the first time, the growth of inhomogeneous thin films by plasma-enhanced chemical vapor deposition (PECVD) using computer-control of the flow rates of the reactant gases. The PECVD technique has several advantages over the codeposition and IAD techniques; these include fast deposition rates, compositional and thickness uniformity, ease of compositional control via a mass flowmeter, and less physical impact damage due to ion bombardment during deposition. The compositionally inhomogeneous dielectric layers realized by PECVD are silicon-oxynitride(SiON)

films. The gases used for growing the inhomogeneous SiON layers are SiH_4, N_2, and N_2O. While the flowrates of SiH_4 and N_2 are kept constant ,real-time control of the N_2O flowrate is achieved using a Techware PAL-68000 process controller. Linearly-graded and superlattice-like SiON layers are fabricated by computer-controlled PECVD with refractive indices varying from 1.48 to 2.05. The compositional profile of the inhomogeneous layers is analyzed by Auger electron spectroscopy(AES) sputter profiling[25]. As an additional proof of the viability of these inhomogeneous films, rugate filters[11,13,18,19,22, 23] are designed, fabricated, and tested.

The second purpose of the research presented herein is to provide examples of possible applications of inhomogeneous films grown by PECVD. Antireflection (AR) coatings[6,7,9,10,13,26-32] and rugate filters with the inhomogeneous refractive index profiles are designed and fabricated. Alternating-current thin-film electroluminescent (ACTFEL) devices[33-38] are designed and fabricated for improved optical characteristics by employing multiple dielectric layers.

An outline of the thesis is as follows. A review of the literature of the analysis, synthesis, and fabrication of single-, multiple-layer, and inhomogeneous optical filters is presented in Chapter 2. Experimental procedures used for the fabrication and characterization of PECVD

thin films are described in Chapter 3. Theoretical and experimental results of inhomogeneous AR coatings and rugate filters are presented in Chapter 4. Subsequently, the design and fabrication of ACTFEL devices with PECVD SiON dielectrics is presented in Chapter 5. Finally, Chapter 6 includes conclusions of this research and recommendations for future research.

Chapter 2. Literature Review

Layered optical media play a very important role in many applications of optics. When a light wave propagates through a single, multiple or inhomogeneous layer dielectric, such as shown in Fig. 2.1, the incident wave may interfere with one or more of the waves that are reflected from the interfaces formed by the thin film and the substrate, and reflection, absorption, and transmission take place as a result. The incident wave may vary in wavelength; in general, reflection, absorption, and transmission are wavelength-dependent. By varying the indices of refraction, thicknesses, and the order of layers, different optical performance can be obtained. Specially designed stacks of dielectric layers are called 'optical filters'. The characteristics of various kinds of optical filters are shown in Fig. 2.2. The three basic issues in optical thin films are analysis, synthesis, and fabrication. Analysis of thin films involves computation of the spectral characteristics of a multilayer with known optical constants and thicknesses. The calculation is quite straightforward using the characteristic matrix of each layer[4,39-42]. The synthesis of optical thin films poses a formidable task.

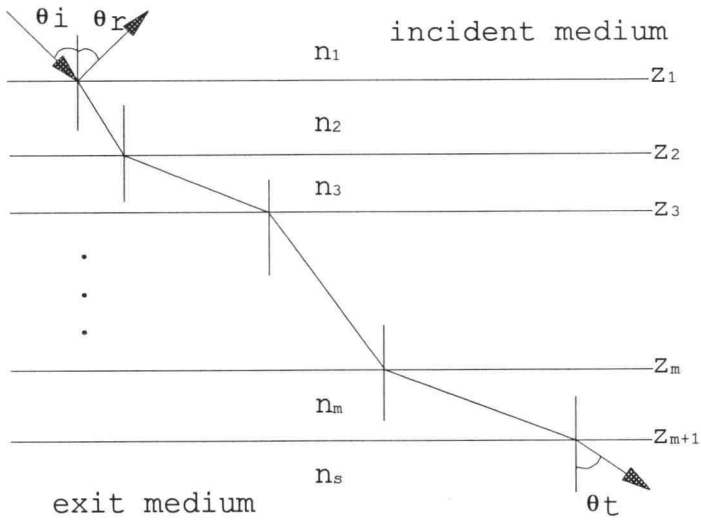

Fig. 2.1 Structure of a multiple dielectric layer.

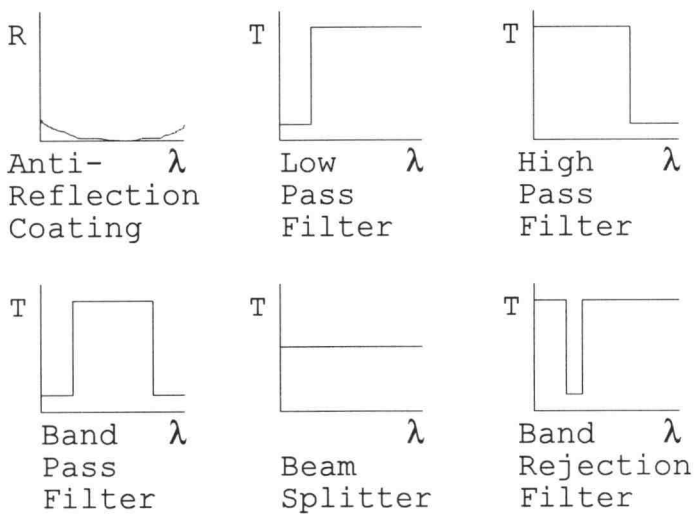

Fig. 2.2 Characteristics of various optical filters[4].

It consists of determining the refractive index and thickness profile of the film so that a specified spectral response is obtained. Due to the development of computers, analytical techniques for designing filters have been replaced by sophisticated computer synthesis programs [43, 44]. However, the limited number of available filter materials makes synthesis more complicated. The development of new techniques for growing inhomogeneous optical thin films in recent years[11-14,25], however, relaxes these constraints so that synthesis and fabrication of optical filters can be achieved.

2.1 The Matrix Method of Thin Film Analysis

When a light wave is incident on a thin film embedded between incident and exit media, reflection and transmission of the light take place. Using the resultant electric and magnetic fields and their boundary conditions, the reflection and transmission of a light wave at the interface of a single or multiple layer film can be derived theoretically and the relationships between incident, reflected, and transmitted waves can be represented as a 2×2 matrix[4,39-42]. It is possible to analyze any thin film structure using this matrix method; a derivation of the matrix method is as follows.

Assume that each layer is nonabsorbing, homogeneous, and isotropic with refractive index n, and assume also that

a linearly polarized electromagnetic wave impinges on a single layer thin film with refractive index n, as shown in Fig. 2.3, between the two surrounding media with refractive indices of n_o and n_s, respectively.

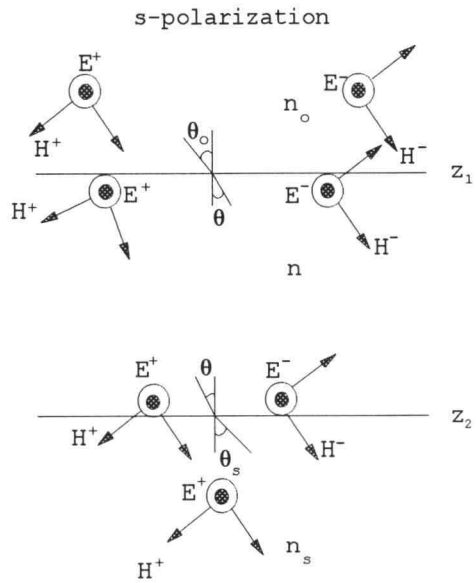

Fig. 2.3 Electromagnetic fields at boundaries. The electric field is perpendicular to the plane of incidence.

Let $E(z_1)$ and $H(z_1)$ be the total electric and magnetic field at $z = z_1$, and $E(z_2)$ and $H(z_2)$ be the total electric and magnetic fields at $z = z_2$. The relationship between the two electromagnetic fields is represented as

$$\begin{bmatrix} E(z_1) \\ Z_o H(z_1) \end{bmatrix} = \begin{bmatrix} \cos\phi & j\frac{\sin\phi}{n} \\ jn\sin\phi & \cos\phi \end{bmatrix} \begin{bmatrix} E(z_2) \\ Z_o H(z_2) \end{bmatrix} \qquad (2.1)$$

where $\phi = (2\pi/\lambda_o)ndcos\theta$

λ_o= wavelength of free space

$d = z_2 - z_1$

θ = angle of transmission determined by Snell's law

$(n_o sin\theta_o = nsin\theta)$

Z_o= characteristic impedance of free space

and n should be replaced by $ncos\theta$ for s polarization and by $n/cos\theta$ for p polarization. The characteristic matrix M in Eqn.(2.2) contains only parameters of the film and does not contain those of the surrounding media, i.e.

$$M = \begin{bmatrix} \cos\phi & j\frac{\sin\phi}{n} \\ jn\sin\phi & \cos\phi \end{bmatrix} . \qquad (2.2)$$

When $ndcos\theta = \lambda_o/4$ (i.e. a quater wave thickness), the characteristic matrix M becomes

$$M_{\lambda_0/4} = \begin{bmatrix} 0 & \frac{j}{n} \\ jn & 0 \end{bmatrix} . \qquad (2.3)$$

When $ndcos\theta = \lambda_o/2$ (i.e. a half wave thickness, then M becomes

$$M_{\lambda_o/2} = \begin{bmatrix} -1 & 0 \\ 0 & -1 \end{bmatrix} . \qquad (2.4)$$

Eqns.(2.3) and (2.4), are very important for optical filter design.

If there are a number of layers, then the characteristic matrix can be used to find the relationship between the electric and magnetic fields of adjacent layers. For example, if there is a layer between $z=z_2$ and $z=z_3$, then,

$$\begin{bmatrix} E(z_2) \\ Z_o H(z_2) \end{bmatrix} = M_2 \begin{bmatrix} E(z_3) \\ Z_o H(z_3) \end{bmatrix} . \tag{2.5}$$

In general, if there are m layers then the relationship of the first and last boundary can be described as

$$\begin{bmatrix} E(z_1) \\ Z_o H(z_1) \end{bmatrix} = M_1 M_2 \cdots M_m \begin{bmatrix} E(z_{m+1}) \\ Z_o H(z_{m+1}) \end{bmatrix} = M \begin{bmatrix} E(z_{m+1}) \\ Z_o H(z_{m+1}) \end{bmatrix} \tag{2.6}$$

where $M = M_1 M_2 \ldots M_m$. Because the characteristic matrix of a single layer has real elements in the principal diagonal and pure imaginary elements in the off diagonal, the product of each characteristic matrix of the multiple layer structure can be represented as

$$M = \begin{bmatrix} M_{11} & jM_{12} \\ jM_{21} & M_{22} \end{bmatrix} . \tag{2.7}$$

The electromagnetic wave in the film in Fig. 2.1 is composed of incident, reflected, and transmitted waves which

can be represented as $E^+(z_1-\delta)$, $E^-(z_1-\delta)$, and $E^+(z_{m+1}+\delta)$, respectively, where δ is very small positive number. The relationship between them is described as

$$\begin{bmatrix} E^+(z_1-\delta) \\ E^-(z_1-\delta) \end{bmatrix} = \begin{bmatrix} Q_{11} & Q_{12} \\ Q_{21} & Q_{22} \end{bmatrix} \begin{bmatrix} E^+(z_{m+1}+\delta) \\ 0 \end{bmatrix} . \tag{2.8}$$

where

$$Q_{11} = \frac{M_{11} + j\,M_{21}/n_o + j\,n_s\,M_{12} + n_s\,M_{22}/n_o}{2}$$

$$Q_{12} = \frac{M_{11} + j\,M_{21}/n_o - j\,n_s\,M_{12} - n_s\,M_{22}/n_o}{2}$$

$$Q_{21} = \frac{M_{11} - j\,M_{21}/n_o + j\,n_s\,M_{12} - n_s\,M_{22}/n_o}{2}$$

$$Q_{22} = \frac{M_{11} - j\,M_{21}/n_o - j\,n_s\,M_{12} + n_s\,M_{22}/n_o}{2} .$$

From Eqn.(2.8) the reflection and transmission coefficients, r and t, may be derived as follows:

$$r = \frac{Q_{21}}{Q_{11}} = \frac{M_{11} - j\,M_{21}/n_o + j\,n_s\,M_{12} - n_s\,M_{22}/n_o}{M_{11} + j\,M_{21}/n_o + j\,n_s\,M_{12} + n_s\,M_{22}/n_o} \tag{2.9}$$

and

$$t = \frac{1}{Q_{11}} = \frac{2}{M_{11} + j\,M_{21}/n_o + j\,n_s\,M_{12} + n_s\,M_{22}/n_o} . \tag{2.10}$$

From Eqns.(2.9) and (2.10), reflectance R and transmittance T are described as

$$R = rr^* \quad \text{and} \quad T = \frac{n_s}{n_o} tt^* = 1 - R \tag{2.11}$$

where r* and t* are the complex conjugates of r and t. Consequently T can be derived from Eqns.(2.9), (2.10), and (2.11) and is given by

$$T = 1 - R = \frac{4\, n_o\, n_s}{(n_o M_{11} + n_s M_{22})^2 + (n_o n_s M_{12} + M_{21})^2} \quad . \qquad (2.12)$$

The equations (2.11) and (2.12) derived above form the basis for analysis and synthesis of multiple layer optical filters. Thus, the transmittance and reflectance of an optical thin film can be calculated using the matrix method.

2.2 Synthesis of Optical Coatings

There are various kinds of optical coatings; e.g. AR coatings, high reflectors, beam splitters, edge filters, band pass filters, and band rejection filters. The spectral characteristics of these are shown schematically in Fig. 2.1. Methods of synthesis of these filters are described briefly in the following.

2.2.1 Antireflection (AR) Coatings

AR coatings are used to reduce the reflection from an optical component when light is incident from air, to reduce the reflectance of an interface between two optical media, and to match a coating design optimized for one optical medium into another. Applications of AR coatings include

cathode-ray tubes, solar cells[45-47], photodetectors, semiconductor lasers[48], and so on.

AR coatings can be realized by a simple single layer coating or a multiple layer system[26-32]. However, the ideal AR coating is an inhomogeneous layer with a continuous transition of the refractive index from one medium to another[6,7-9,13]. Because there are few practical optical coating materials with a limited range of refractive indices, and because it is very difficult to grow inhomogeneous layers , normally single or multiple layer structures are used for AR coatings and other optical thin film applications. A list of coating materials with their refractive indices of is given in Table 2.1[4].

The refractive index n of a single layer AR coating on a glass substrate (n_s=1.52) requires that $n=(n_o n_s)^{1/2}$ =1.26 with a quarter wavelength thickness for zero reflectance at a specified frequency. Such a material is not available in Table 2.1. Therefore multiple layer AR coatings have been developed in order to obtain minimum reflectance over a wide bandwidth. Muchmore[26] used a network analysis method to design AR coatings with optimum bandwidths. Young[28] modeled AR coating as a multisection quarter-wave matching network to minimize reflection over a prescribed frequency band. Cox, Hass and Thelen[30] found that quarter-half-quarter triple layer structures provide a broader bandwidth of low reflection than single and double layer structures

for many combinations of indices and thicknesses for a glass substrate.

Table 2.1 Ranges of transparency and refractive indices of some coating materials[4].

Material	Refractive index at the λ below(in μm) 0.35	0.55	1.0	1-8	10	Range of Transparency (in μm)
Ge				4.2	4.2	1.7-25
Si			3.9	3.42		1.0-9
TiO2		2.32	2.20			0.4-6
ZnS		2.36	2.27	2.24		0.4-14
ZrO2	2.15	2.05	2.0			0.3-
Ta2O3	2.31	2.16	2.09			0.3-
SiO		2.0	1.9	1.85		0.5-8
Al2O3	1.66	1.63	1.60			0.15-9
Si2O3		1.57	1.55			0.3-8
SiO2	1.48	1.46	1.45			0.16-8
MgF2	1.39	1.38		1.36		0.13-1
Cryolite		1.30-1.35				0.13-9

2.2.2 Periodic Multiple Layer Structures

Different approaches are employed for the design of optical interference filters. According to Herpin[39] a symmetrical thin film combination is equivalent to a single layer characterized by an equivalent index of refraction and thickness. Epstein[49] showed that the equivalent index of refraction N and thickness Γ of a symmetric film could be represented as

$$N = \sqrt{\frac{M_{21}}{M_{12}}} \tag{2.13}$$

and

$$\cos \Gamma = M_{11} = M_{22} \tag{2.14}$$

because the resultant characteristic matrix of a symmetrical layer has the same diagonal elements. The particular structures of interest are three layer combinations of the form ABA where the two outer layers have the same refractive index and thickness. When there are p periodic ABA layers, the characteristic matrix, M, with an equivalent index, N_{ABA}, and an equivalent thickness, Γ_{ABA}, of the layer depends on whether N_{ABA} is real or imaginary. When N_{ABA} is real M is written as

$$M = \begin{bmatrix} \cos p\Gamma_{ABA} & j\dfrac{\sin p\Gamma_{ABA}}{n_{ABA}} \\ j\, n_{ABA} \sin p\Gamma_{ABA} & \cos p\Gamma_{ABA} \end{bmatrix} \tag{2.15}$$

and when N_{ABA} is imaginary M becomes

$$M = \begin{bmatrix} \cosh p\Gamma_{ABA} & j\dfrac{\sinh p\Gamma_{ABA}}{n_{ABA}} \\ j\, n_{ABA} \sinh p\Gamma_{ABA} & \cosh p\Gamma_{ABA} \end{bmatrix} . \tag{2.16}$$

For example, the equivalent index, N, and the equivalent thickness, Γ, of the (L/2)H(L/2) and (H/2)L(H/2) structure

with n_L=1.45 and n_H=2.25 are shown in Figs. 2.4 and 2.5. From these figures it is evident that multiple periodic structure display band pass or band stop characteristics according to whether N_{ABA} is real or imaginary. These periodic multilayer structures may be imployed to realize band rejection filters, bandpass filters, edge filters, beam splitters, and so on.

The use of non-symmetric periodic multilayer structures is sometimes desirable. Herpin[39] showed that non-symmetric layers are equivalent to two films. By adding and removing H/2 or L/2 layers, a non-symmetrical periodic multiple layer can be changed into a symmetric multilayer structure[4]. Southwell[32] showed that a very thin two dielectric layer

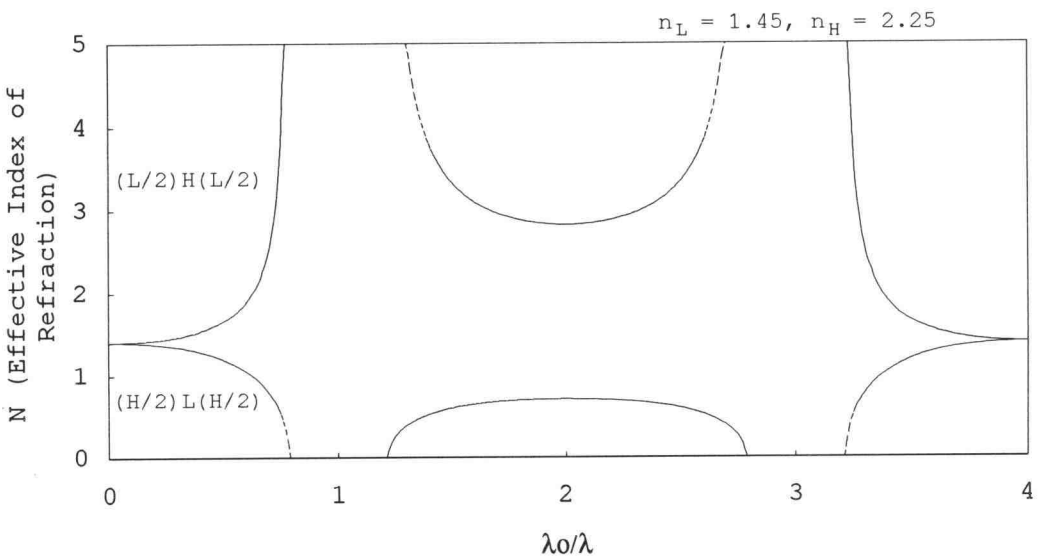

Fig. 2.4 Equivalent index of symmetrical thin-film combinations[49].

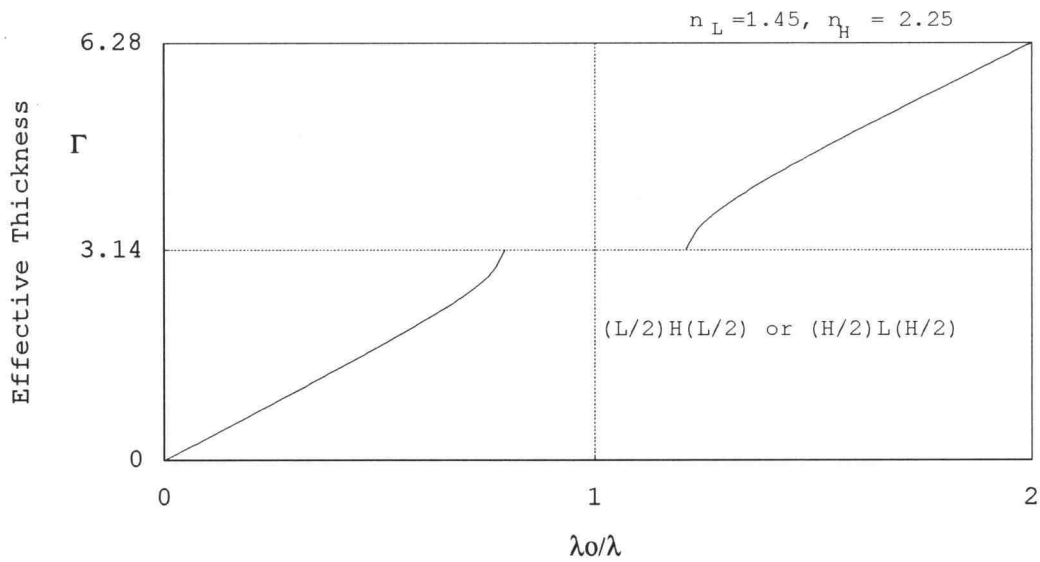

Fig. 2.5 Equivalent thickness of symmetrical thin-film combinations[49].

is equivalent to a single layer structure. Therefore, symmetric periodic multiple layer structures are the basic building block for the realization of various kinds of optical filters[1-5,50-58].

The problem of designing multiple layer filters with specified reflectance or transmittance properties is very complex and there is no simple method of solution applicable to all kinds of filters, even though there are some basic structures which are useful as building-blocks for optical filter synthesis. Typically, severe restrictions such as equal optical thickness, periodicity, symmetry, and the refractive index of each layer are imposed on the filter design in order to reduce the complexity.

The development of digital computers has enabled the filter designers to lift some of restrictions discussed above so that filters with improved performance may be designed. The performance of an optical filter may be evaluated by simulating the spectral response of a filter and comparing it to the desired spectral response so that a suitable "merit function" may be designated.

Baumeister[43] used a successive approximation method for the design of optical filters. Small changes were made iteratively in the design variables in order to produce a better approximation to the desired result from an initial design. The change in reflectance, ΔR_j, or transmittance, ΔT_j, of an N layer filter at a specified frequency by changing the layer thickness by Δd_i is given by

$$\Delta R_j = -\Delta T_j = \sum_{i=1}^{N} \frac{\partial R_j}{\partial d_i} \Delta d_i + O(\Delta d_i)^2 \qquad (2.17)$$

if the refractive indices remain constant. However, Baumeister's refinement process always requires the designer to begin with an original structure whose spectral response is a reasonable approximation to that desired. Dobrowolski [44] used an exhaustive search method in which the designer does not have to specify an original design. Heavens and Liddel[2] improved Dobrowolski's method by reducing the computer time for finding the optimized merit function.

2.2.3 Fourier Transform Method of Synthesis

Certain design procedures require restrictions such as equal optical thickness, periodicity, or symmetry of the refractive index of the layers in the synthesis of multiple layer filters. If these restrictions are removed, the optical filter designer would have more degrees of design freedom.

Sossi[15,16] developed a Fourier transform method for the design of interference coatings having a given transmittance function, T(k), where k is the wave number. In contrast to the above mentioned methods, there are no required assumptions about the number of layers, thicknesses, or refractive indices. The starting point is the transmittance, T(k), of an inhomogeneous film in terms of the refractive index, n(x), where x is twice the optical path inside the film. A refractive index profile as a function of position can be obtained for an inhomogeneous layer of infinite extent which may then be approximated by a finite system of discrete homogeneous layers.

Sossi proved that the spectral transmittance of an inhomogeneous layer is related to its refractive index profile by the following approximate expression

$$\int_{-\infty}^{+\infty} \frac{dn}{dx} \frac{1}{2n} e^{jkx}\, dx = Q(k)\, e^{j\phi(k)} = f(k) \qquad (2.18)$$

where $k=2\pi/\lambda$, $Q(k)$ is an even function of the desired transmittance, x is the twice the optical path,

$$x = 2\int_0^z n(u)du \ , \tag{2.19}$$

and $\phi(x)$ is the phase factor. From Eqn. (2.18), $n(x)$ can be derived as

$$n(x) = \exp\left(\frac{\pi}{2}\int_0^\infty \frac{Q(k)}{k}\sin(\phi(k) - kx)dx\right) \ . \tag{2.20}$$

The success of this method depends on obtaining a good approximation for $Q(k)$, an even function of the desired transmittance. Dobrowolski[17], following Sossi, defined $Q(k)$ as

$$Q(k) = \left[\frac{1}{2}\left(\frac{1}{T(k)} - T(k)\right)\right]^{\frac{1}{2}} \tag{2.21}$$

and he showed several examples of filters designed using Eqn. (2.21). He also combined the Fourier transform method with his completely automatic synthesis method[44] to convert the inhomogeneous index profile to a multiple layer structure, using a limited range of refractive indices. Biovin and St.-Germain[21] designed band rejection filters of narrow bandwidth using Eqn. (2.21). Because of discrepancies of the spectral response between the results

of the Fourier transform method and the matrix method, Bovard[22] modified the Fourier transformation method to reduce the error in designing band rejection filters with narrow bandwidth.

In order to reduce the errors inherent to the Fourier transform method, including the inaccuracy of the spectral function Q(k), Verly and Dobrowolski[24] applied a numerical compensation method by successive approximation. They showed that the complex phase of Q(k) is the key parameter which can be exploited to reduce significantly the thickness of the synthesized film and to control the shape of the refractive index profile without affecting the spectral performance.

2.3 Fabrication of Inhomogeneous Optical Coatings

There are numerous synthesis techniques for the design of inhomogeneous optical coatings[15-18,21-24] which have been developed for over a period of 30 years [6,8]. However, the realization of inhomogeneous optical coating has been hampered by the lack of fabrication technologies. Recently the development of computer-controlled fabrication technologies has allowed continuous control of process parameters so that inhomogeneous optical coatings may be realized[7,10,13,14,21,25].

Jacobsson[6,7,9] proposed the use of inhomogeneous optical coatings to reduce the reflectance of AR coatings.

He used vacuum co-deposition in order to generate a film with an intermediate refractive index. This is a very difficult process to implement because it is very hard to control simultaneously the necessary process parameters such as the temperature and deposition rate of all of the sources.

Boivin and St.-Germain[21] used the coevaporation method in which the rate of deposition of the low index material is kept constant while the rate of the high-index material is controlled by an automatic shutter that delivers a rate of deposition proportional to a preset reference function. The reference function, corresponding to a desired index profile, is stored in memory and as the deposition progresses the rate controller delivers the appropriate amount of material in the mixture so as to produce the desired refractive index. However, the range of refractive index available is very small because it is limited by the constant evaporation rate.

Electron-beam evaporation using two computer-controlled electron-beam sources has been used to grow inhomogeneous layers[12,13]. Ion beam cosputtering was also used to grow inhomogeneous films of TiO_2 and SiO_2 by reactive sputtering of titanium and silicon targets[13]. However, oxides formed on the target surface significantly reduced the sputtering rates, particularly that of titanium. The most recent method reported for the growth

of inhomogeneous layers is ion assisted deposition[14]. The compositional variation of the film was realized by reactive ion beams through control of the relative gas fluxes.

Compared to the above mentioned physical vapor deposition(PVD) methods chemical vapor deposition(CVD) method has not been used for growing inhomogeneous dielectric layers. PECVD is one such CVD technique and it has advantages over PVD methods. The thickness of the film is more uniform and the physical damage on the film surface due to the collision of accelerated ions can be minimized in film grown by PECVD. It is also possible to obtain compositional variation of the film by controlling the flow rates of gases in the PECVD process.

2.4 Rugate filters

One possible application of the inhomogeneous thin films discussed above is a rugate filter which reflects incident light waves over a certain band of wavelengths. A rugate filter[13,19,22,59,60] is an optical coating in which the refractive index varies sinusoidally throughout its thickness. Baumeister simulated a rugate filter via a stepped-index dielectric multilayer[19]. Bovard also derived a matrix describing a rugate thin film[22]. Instead of using the stepped index approximation, Southwell[59] and Yeh[60] calculated the spectral response of the rugate filter using

coupled-mode wave theory. By modulating the envelope of the sinusoidally varying refractive index, almost ideal band rejection characteristics were achieved theoretically[22,23, 61]. Therefore, the fabrication of rugate filters is one of the more complex applications of inhomogeneous optical coatings and is considered to be a proof of the growth of an inhomogeneous dielectric layer. The theoretical analysis of a rugate is described as follows[59,60].

The propagation of a light wave along the z axis in an inhomogeneous layer with a refractive index n = n(z) is given by

$$\frac{d^2 E(z)}{d z^2} + \left[\frac{\omega}{c} n(z)\right]^2 E(z) = 0 \qquad (2.22)$$

where ω is the angular frequency and c is the velocity of light in free space. The exact solution of Eqn. (2.22) can be given when n(z) is a linear, exponential, or hyperbolic function. When the closed form solution of Eqn.(2.22) is not available, the inhomogeneous layer can be replaced by a large number of homogeneous layer films and the reflectance and transmittance can always be obtained using the matrix method, as described in section 2.1.

Consider a rugate filter in which the refractive index varies sinusoidally as a function of position. The refractive index profile of a rugate filter is shown in Fig. 2.6. The refractive index of Fig. 2.6 is expressed as

$$n(z) = n_o + n_1 \cos(Kz) \tag{2.23}$$

where

$$K = \frac{2\pi}{\Lambda} \tag{2.24}$$

and Λ is the thickness of one sinusoidal layer.

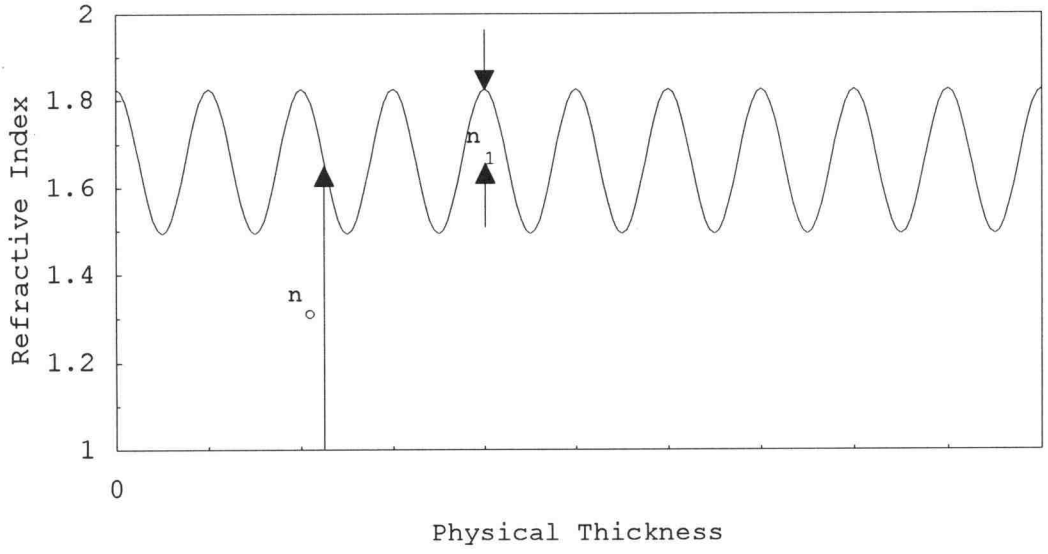

Fig. 2.6 Refractive index profile of a rugate filter.

Using the assumption that $n_1 << n_o$ and neglecting the small second order term, the wave equation for the rugate filter reduces to

$$\frac{d^2 E(z)}{d z^2} + \frac{\omega^2}{c^2}(n_o^2 + 2 n_o n_1 \cos Kz)E(z) = 0 \quad . \qquad (2.25)$$

Using coupled-mode analysis, the solution of Eqn.(2.25) can be written as

$$E(z) = A(z)\, e^{-jk_o z} + B(z)\, e^{jk_o z} \qquad (2.26)$$

where $e^{-jk_o z}$ and $e^{jk_o z}$ are normal modes of the unperturbed structure with k_o given by

$$k_o = \frac{2\pi n_o}{\lambda} = \frac{\omega}{c} n_o \quad . \qquad (2.27)$$

Substituting Eqn.(2.26) into the wave equation and using the parabolic approximation with spatial average, we have

$$A' = -j \frac{\omega n_1}{2c} B\, e^{j(2k_o - K)z} \qquad (2.28)$$

and

$$B' = j \frac{\omega n_1}{2c} A\, e^{-j(2k_o - K)z} \quad . \qquad (2.29)$$

The condition for having Eqns. (2.28) and (2.29) is

$$2 k_o \cong K \qquad (2.30)$$

By defining a coupling constant k as

$$\kappa = \frac{\omega n_1}{2c} = \frac{\pi n_1}{\lambda} \tag{2.31}$$

and

$$\Delta k = 2 k_o - K \tag{2.32}$$

and from the coupled equations Eqns. (2.28) and (2.29)

$$A'' - j\Delta k A' - \kappa^2 A = 0 \ . \tag{2.33}$$

The solution of Eqn. (2.33) can be written as

$$A(z) = [C_1 \cosh sz + C_2 \sinh sz] e^{j(\Delta k/2)z} \tag{2.34}$$

where C_1 and C_2 are constants and s is given by

$$s^2 = \kappa^2 - \left(\frac{\Delta\kappa}{2}\right)^2 \ . \tag{2.35}$$

B(z) is obtained by the same procedure.

Now let a light wave be incident normally on the film at z=0, then the reflection coefficient r is given by

$$r = \frac{B(0)}{A(0)} \ . \tag{2.36}$$

Since the light is incident from the left at z=0, the boundary condition for the reflected light at z=L is

$$B(L) = 0 \ . \tag{2.37}$$

Using the above boundary conditions A(z) and B(z) are expressed as

$$A(z) = \frac{s\cosh s(L-z) + j(\frac{\Delta k}{2})\sinh(L-z)}{s\cosh L + j(\frac{\Delta k}{2})\sinh sL} A(0)\, e^{j(\Delta k/2)z} \tag{2.38}$$

and

$$B(z) = \frac{-j\kappa \sinh sL}{s\cosh L + j(\frac{\Delta k}{2})\sinh sL} A(0)\, e^{-j(\Delta k/2)z} \ . \tag{2.39}$$

From Eqns. (2.36), (2.37), and (2.39) the reflection coefficient becomes

$$r = \frac{-j\kappa \sinh sL}{s\cosh sL + j(\Delta k / 2)\sinh sL} \tag{2.40}$$

Also the reflectance R = r*r and can be expressed as

$$R = \frac{\kappa^2 \sinh^2 sL}{s^2\cosh^2 L + (\Delta k/2)^2 \sinh^2 sL} \tag{2.41}$$

From Eqn. (2.41) the reflectance maximum can be obtained when $\Delta k = 0$ and it is expressed as

$$R = \tanh^2 \kappa L \ . \tag{2.42}$$

The reflectance R in Eqn. (2.42) approaches unity when κL is large. The bandwidth of the main peak is given approximately by

$$\Delta k = 4\kappa \tag{2.43}$$

and the calculated bandwidth $\Delta\lambda$ is given by

$$\frac{\Delta\lambda}{\lambda_o} = 2\left|\frac{n_1}{n_o}\right| \ . \tag{2.44}$$

Thus, the closed-form solution to the wave equation for a rugate filter is derived on the basis of coupled-mode theory. The design of a rugate filter can be accomplished using Eqns. (2.24), (2.30), and (2.44); an example of a rugate filter design using these equations is presented in section 4.3.1.

Chapter 3. Experimental Procedure

In this chapter the PECVD and PAL-68000 systems used to grow multiple and inhomogeneous dielectric SiON layers are described. Additionally, ellipsometry, Auger electron spectroscopy (AES), and transmission measurements using a spectrophotometer are described, which are used to characterize the physical and optical properties of the SiON films grown by PECVD. Finally, the methods of electrical characterization of SiON films and ACTFEL devices are presented.

3.1. PECVD system with a PAL-68000 Process Controller

3.1.1 PECVD

PECVD differs from conventional pyrolitic chemical vapor deposition (CVD) which uses purely thermal activation of the deposition reaction at very high temperatures, typically in excess 800°C. Instead, PECVD uses a plasma to activate or enhance the deposition reactions to produce thin films from flowing reactant gases[62-68] (A plasma is a partially ionized gas consisting of equal number of positive and negative charges as well as including a large number of netural particles[69]). Therefore, PECVD can be accomplished at a reduced substrate temperature, typically about 300°C. The

physical properties of plasma-deposited films depend on process parameters which modify the plasma properties such as pressure, substrate temperature, power, plasma excitation frequency, and gas flow rates.

A schematic diagram of the Semigroup 1000 PECVD system, which is used to grow SiON layers, is shown in Fig. 3.1. The PECVD reactor has a capacitively coupled, parallel plate configuration in which the top electrode is powered, while the bottom electrode is grounded and heated. The reaction chamber, made of aluminum, is 43 cm in diameter and

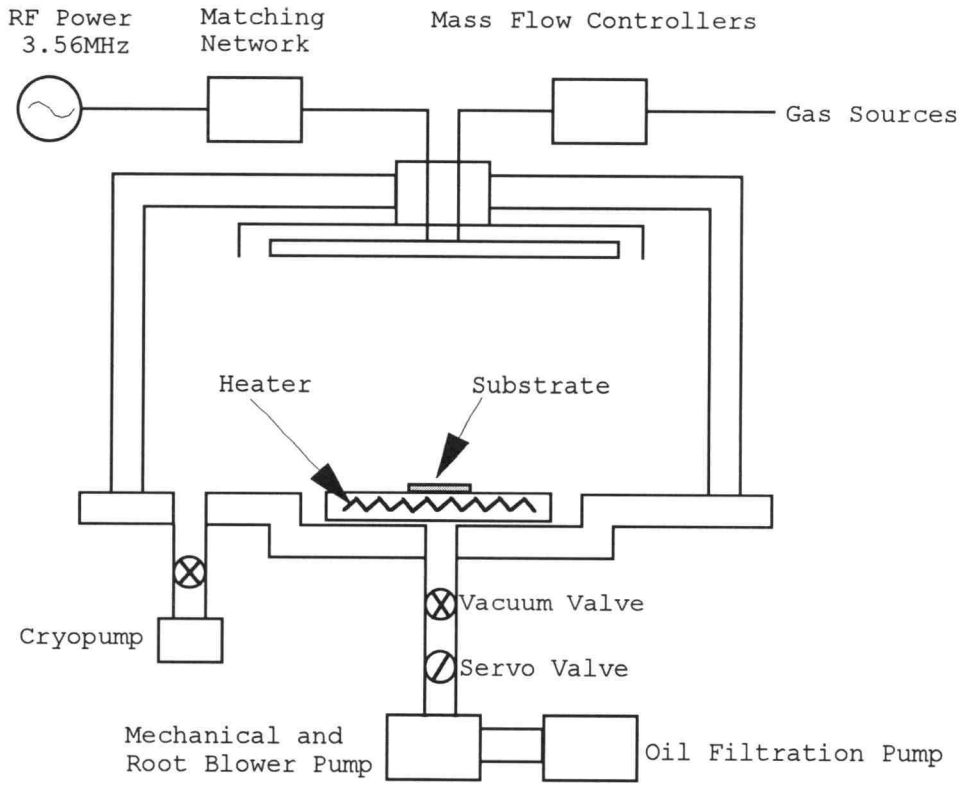

Fig. 3.1 A schematic diagram of the PECVD system

the distance between the top and the bottom electrodes is 10.2 cm. A steady state glow discharge plasma is achieved between the two electrodes by RF excitation while the reactant gases flow through the PECVD chamber. The RF power is coupled to the top electrode via an impedance matching network and the forward and reflected RF powers are monitored with a built-in power meter. The system has a built-in microprocessor for semi-automatic control of process parameters so that the pressure, RF power, gas flowrates, substrate temperature can be maintained constant during the operation of the system.

The SemiGroup 1000 PECVD system is used to grow SiON layers. An excitation frequency of 13.56 MHz, substrate temperature of 300°C, chamber pressure of 500 mTorr, and power density of about 165mW/cm^2 is used. Silane (SiH_4) diluted in helium (2.01% SiH_4 in He), nitrogen (N_2), nitrous oxide (N_2O) diluted in helium (5% N_2O in He) are the process gases employed for the growth of SiON layers. It is reported that high quality SiON films can be grown by using helium-diluted reactant gases in PECVD[78-80]. N_2O is exceedingly reactive, compared to N_2, so that small variations of the N_2O flow rate result in large variations in the refractive index of the film. For this reason, the flow rates of SiH_4 and N_2 (as well as other deposition parameters such as RF. power, chamber pressure, and substrate temperature) are kept constant using the

SemiGroup programmable microprocessor; only the N_2O flow rate is subject to real time control via a Techware PAL-68000 process controller.

3.1.2 PAL-68000

The physical properties of a PECVD grown dielectric layer can be varied by changing the values of the process parameters. It is possible to grow inhomogeneous dielectric layers if the gas flow rate is varied continuously as a function of time. A Techware PAL-68000 [70] process automation controller is connected to the PECVD system in order to control the flow rate of N_2O continuously as a function of time. The PAL-68000 is a real-time, multi-tasking process control system used for the automation of thin film deposition and etching processes. The PAL-68000 uses PAL, a specially designed language for programming process equipment. A PAL program is written to create a process sequence and parameter setpoints according to user-defined requirements.

The PAL-68000 system is a very flexible controller with 12 analog and 12 digital input and output channels. PECVD process parameters such as chamber pressure, gas flow rates, and RF power can be connected to analog channels, while valves and switches can be controlled by digital channels of the PAL-68000 system. Each channel is preassigned for a prescribed function using a

configuration file of the system. Channels are used to define the state of a particular input/output point. All channels are defined as bi-directional. That is , they may contain a "value" or a "setpoint." A value is defined as a state which originates at a component in the PECVD system and is supplied to the PAL-68000 system. A setpoint is defined as a state which originates from the PAL-68000 system and is supplied to the process equipment. A schematic diagram of the PAL-68000 controller is shown in Fig. 3.3.

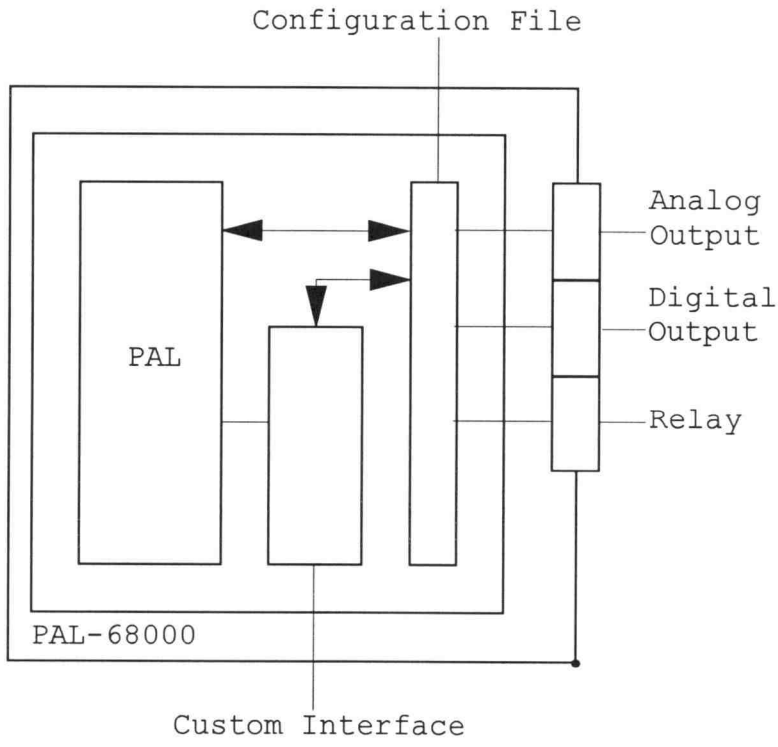

Fig. 3.2 Block diagram of the PAL-68000 automatic process controller.

3.1.3 Coupling of the PECVD to the PAL-68000

In order to utilize the PAL-68000 system to control the PECVD system, a mass flow controller (MFC) for N_2O with maximum flow rate of 500 sccm is chosen as an analog output channel for the PAL-68000 system. An MFC is a device which controls the flow rate of a reactant gas of the PECVD process. The model number of the MFCs used are MKS 2259B[71]. The model 2259B MFC accepts a 0-5 V (DC) setpoint signal and the flow rate of a gas flowing through this MFC is proportional to the setpoint voltage. The response time of the 2259B MFC is less than 2 seconds and is accurate to within ±2% of a setpoint value. The setpoint voltage for the 2259B MFC is kept constant for the growth of homogeneous SiON layers.

It is possible to change the flow rate of a certain gas during thin film deposition by controlling the setpoint voltage applied to the 2259B MFC. Real time control of the setpoint voltage of the 2259B MFC is achieved using the PAL-68000 system. An analog output channel is assigned to the PAL-68000 to generate a setpoint voltage for the 2259B MFC for N_2O gas. A PAL program is created for the required flow rates and deposition time to grow multilayer or inhomogeneous dielectric films. The poll period, during which the PAL-68000 system reads or writes the value of each channel, varies from 1/8 to 8 seconds and is taken into account in

creating the process program. A schematic diagram of PECVD with PAL-68000 is shown in Fig. 3.3.

An example of a PAL program for the growth of an AR coating is shown in Table 3.1. In this example, three analog channels and one digital channel are selected to be controlled by the PAL-68000 system. The analog channels

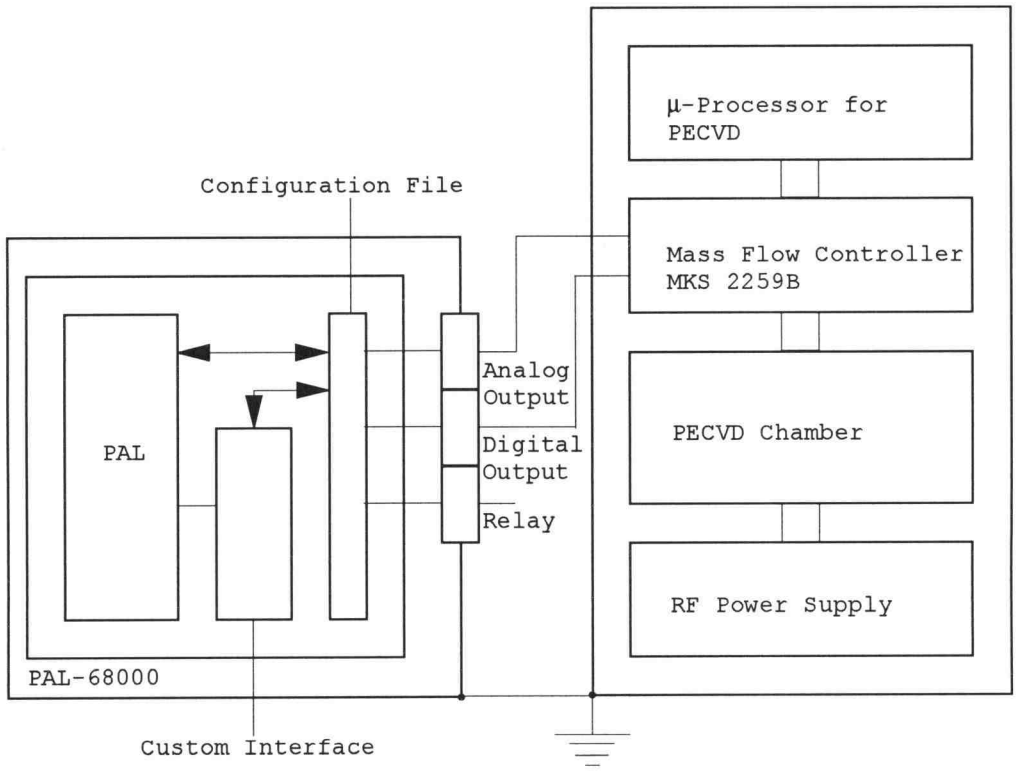

Fig. 3.3 MKS 2259B MFC of the PECVD system is connected to the PAL-68000 automatic process controller.

are the N_2O flow rate and RF power defined as flow-setpt and power, respectively. A digital channel defined as "Valve" is for the opening and closing of the 2259B MFC.

The other process parameters of the PECVD system are assumed constant. In this table, seconds and flow.setpt are chosen from the experimental calibration chart

Table 3.1 An example of a PAL program for a multiple layer AR coating.

EVENT	ACTION
Sequence /AR	None
Always	Valve = Op
Always	**Comment** AR coating
When d:seconds > 10 sec	flow.sept = 294.74 sccm
When d:seconds > 60 sec	Power = 70 W
When d:seconds > 250 sec	flow.sept = 0.00 sccm
When d:seconds > 873 sec	flow.sept = 9.01 sccm
When d:seconds > 30 sec	flow.sept = 12.28 sccm
When d:seconds > 525 sec	flow.sept = 18.83 sccm
When d:seconds > 570 sec	flow.sept = 26.20 sccm
When d:seconds > 12 sec	flow.sept = 34.39 sccm
When d:seconds > 263 sec	flow.sept = 43.39 sccm
When d:seconds > 276 sec	flow.sept = 54.04 sccm
When d:seconds > 469 sec	flow.sept = 67.14 sccm
When d:seconds > 154 sec	flow.sept = 83.51 sccm
When d:seconds > 239 sec	flow.sept = 103.16 sccm
When d:seconds > 197 sec	flow.sept = 124.45 sccm
When d:seconds > 457 sec	flow.sept = 152.29 sccm
When d:seconds > 363 sec	flow.sept = 0.00 sccm
Always	Power = 0 W
Always	Valve = Cl
Always	End of /AR

discussed in Chapter 4. The expected refractive index profile and thickness are shown in Fig. 4.10 (a).

3.2. Characterization Techniques

The three major techniques used for the physical and optical characterization of inhomogeneous SiON films grown by computer-controlled PECVD are ellipsometry[72,73], Auger electron spectroscopy (AES) [72,74,75], and optical transmission using a spectrophotometer[72]. The ACTFEL characterization techniques used in this experiments are capacitance-voltage (C-V)[38,76,77,78], internal charge-phosphor electric field (Q-F_p)[79,80], and luminance-voltage (L-V)[81] measurement. The principles of operation of each technique are described as follows.

3.2.1. Ellipsometry

Ellipsometry[81] is used to generate the calibration chart of the SiON films. Homogeneous SiON films under different gas flow rate are grown on silicon substrates. Their thicknesses and refractive indices are measured by ellipsometry. Ellipsometry[81] is based on measuring the state of polarization of polarized light. Ellipsometric measurements[83] involve illuminating the surface of a sample with monochromatic light having a known, controllable state of polarization and then analyzing the polarization state of the reflected light. When light is

reflected from a single surface, it is generally reduced in amplitude and shifted in phase. For a multiple reflecting surface, the various reflecting beams interfere with one another which results in an amplitude variation as a function of wavelength and incident angle. Therefore it is possible to deduce optical variables such as refractive index and thickness from an ellipsometric measurement.

Assume that plane-polarized light is incident on a flat surface. The electric field of the linearly polarized light can be resolved into p and s components as

$$\vec{E} = E_p \hat{p} + E_s \hat{s} \tag{3.1}$$

where the p component, E_p, is parallel to the plane of incidence and the s component, E_p, is vertical to the plane of incidence and where $\hat{p}$ and $\hat{s}$ are unit vectors parallel and vertical to the plane of incidence, respectively. The reflection coefficients, R_p and R_s of each p and s component can be written as

$$R_p = \frac{E_p(\text{reflected})}{E_p(\text{incident})}, \quad \text{and} \quad R_s = \frac{E_s(\text{reflected})}{E_s(\text{incident})}. \tag{3.2}$$

R_p and R_s are not measurable, but the complex reflection ratio ρ can be defined in terms of ellipsometric angles Ψ ($0° \leq \Psi \leq 90°$) and Δ ($0° \leq \Delta \leq 360°$) as follows.

$$\rho = \frac{R_p}{R_s} = \tan(\Psi)e^{j\Delta} \tag{3.3}$$

$$\Psi = \tan^{-1}\left(\frac{R_p}{R_s}\right) \tag{3.4}$$

where

$$\Delta = \Delta_p - \Delta_s = \text{differential phase change,} \tag{3.5}$$

and Ψ and Δ are the most commonly employed ellipsometer variables and are used to determine the sample optical parameters. The most important application of ellipsometry is to measure the refractive index, n_1, of a nonabsorbing insulator film deposited on a highly absorbing substrate with a known complex refractive index of $n_2 - jk_2$. n_1 and the film thickness can be calculated from the results of single Ψ and Δ measurement[83]. Because of the complexity of equations involved in the computation of the refractive index and thickness, these parameters are evaluated numerically.

A schematic diagram of a rotating analyzer ellipsometer used to measure Ψ and Δ is shown in Fig. 3.4.

The light from the laser source is depolarized to achieve a circular polarization of the beam. After it passes through the polarizer, the circularly polarized light is converted to a linearly polarized beam. The reflected light subsequently becomes elliptically polarized because its polarization is altered by the optical properties of the sample. The reflected light then passes through a rotating analyzer prism and is sensed by a photodetector which, in turn, converts the light power into an electric current proportional to the intensity of the reflected light passing through the analyzer. An optical interference filter between the analyzer and photodetector

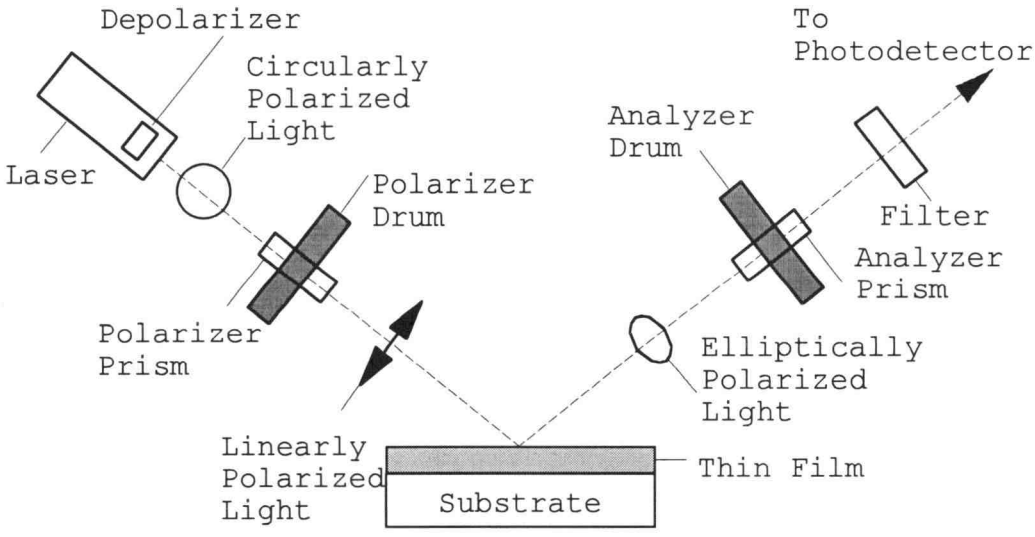

Fig. 3.4 Optical system functional diagram of rotating analyzer ellipsometer.

blocks out all wavelengths other than that of the laser beam, eliminating the effects of ambient illumination. Finally, the refractive index and thickness of the film are calculated numerically via a desktop calculator using Ψ and Δ as input data.

3.2.2. Auger Electron Spectroscopy (AES)

AES is used to verify the compositionally graded SiON films by sputter profiling. AES[81,82,86] is a surface analytical technique useful for the study of the chemical composition of thin films. All elements except hydrogen and helium can be detected using AES. Although the basic Auger technique samples a depth of typically 5 to 50 Å, it is possible to obtain depth information by sputter etching the samples.

AES detects emitted Auger electrons for analysis. The process of Auger electron emission is illustrated in Fig. 3.5. Auger electrons are emitted from the atom as the result of the ionization of an inner shell electron and the coupling of deionization energy associated with the filling of this inner core state to an electron in an outer shell. Auger electrons in AES arise from electron beam ionization and provide a distinctive signature which allows chemical interpretation to be accomplished. The energy spectrum of Auger electrons is characteristic of each atom and is independent of the incident electron

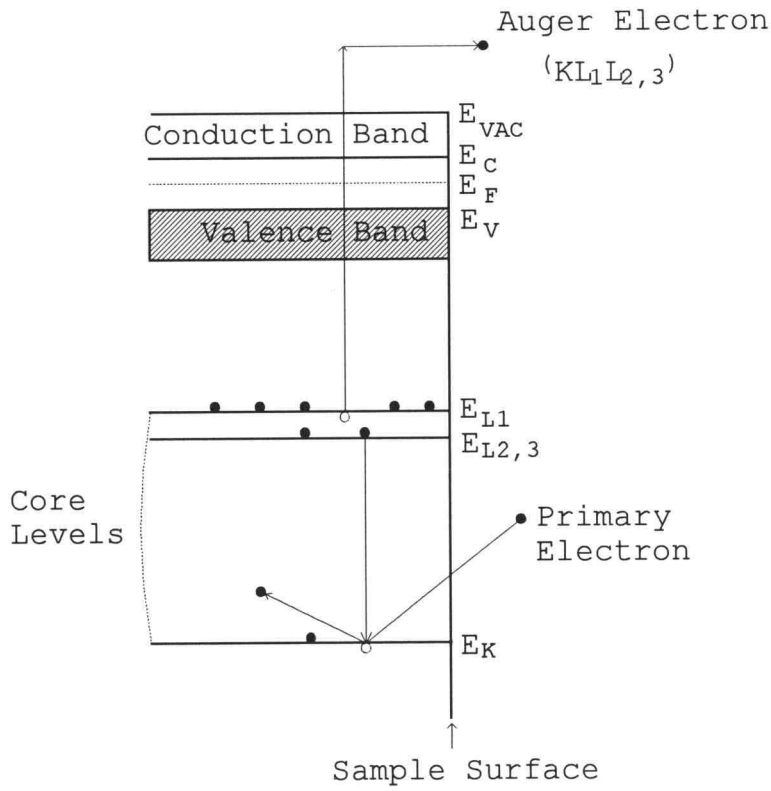

Fig. 3.5 Electronic process in AES.

energy. Emitted Auger electrons are detected and analyzed by an electron energy analyzer. The energies of Auger electrons vary typically from 30 to 3000 eV. A schematic diagram of an AES system is shown in Fig. 3.6.

An AES system basically consists of an electron gun, an electron energy analyzer, a sputter ion gun for depth-profiling, and control circuits. A 1-5 KeV electron beam is incident on the surface of the sample under very high vacuum conditions. The high energy electron beam produces Auger electrons which are detected by the electron energy

analyzer. Auger electrons enter the inlet aperture between two concentric cylinders and arrive at the electron multiplier detector. Final results of the analysis are the Auger electron spectra as a function of the electron energy.

A depth profile of a thin film can be achieved by AES sputter profiling. The sample to be analyzed is bombarded with ions from an ion gun at a typical energy of 1 KeV. A small fraction of the ion energy is transferred to surface atoms and causes them to be sputtered away as Auger electrons being analyzed. The final result of an AES depth profile is a plot of the atomic concentration as a

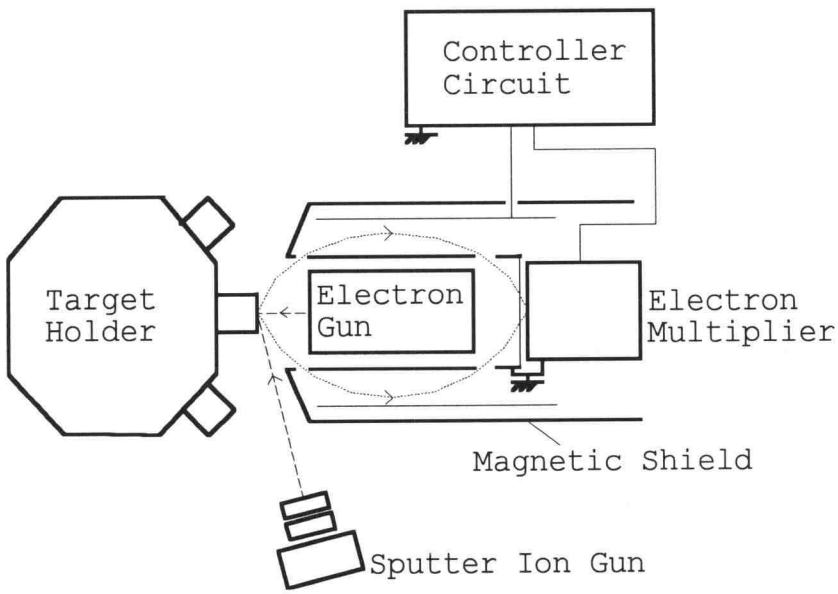

Fig. 3.6 Schematic diagram of an Auger electron spectroscopy system.

function of sputtering time which then can be converted to thickness.

One problem associated with AES depth profiling, relevant to the work presented herein, involves knock-on effects[82] caused by sputtering ions such as Ar^+ which result in atomic mixing so that depth profiles are smeared and appear continuous even at abrupt junctions. The sputtering ion pushes a fraction of the surface species into the sample rather than sputtering them away; thus, the compositional profile is appears broader in an AES depth profile than it is actually.

3.2.3 Optical Transmission

Optical transmission measurements are used to determine the spectral response of AR coatings, ACTFEL devices, and rugate filters. During transmission measurements light is incident on the sample, and the transmitted light is measured as a function of wavelength.

A Hewlett-Packard (HP) 8452A diode array spectrophotometer[87] is used for optical transmission measurements. A schematic diagram of the HP 8452A system is shown in Fig. 3.7. A source generates light over the 190 nm to 820 nm wavelength range. The source lens receives the light from the lamp and collimates it so that the beam passes through the sample. A spectrograph lens refocuses the light beam after it passes through the

sample. The slit is a narrow aperture in a plate located at the focus of the spectrograph lens. After passing through the slit, light is incident on the grating which separates the light beam into its component wavelengths and reflects the light onto a diode array. The diode array is a series of 328 individual photodiodes and control circuits etched onto a semiconductor chip. Each photodiode monitors a certain wavelength so that the spectral response of a thin optical film can be constructed.

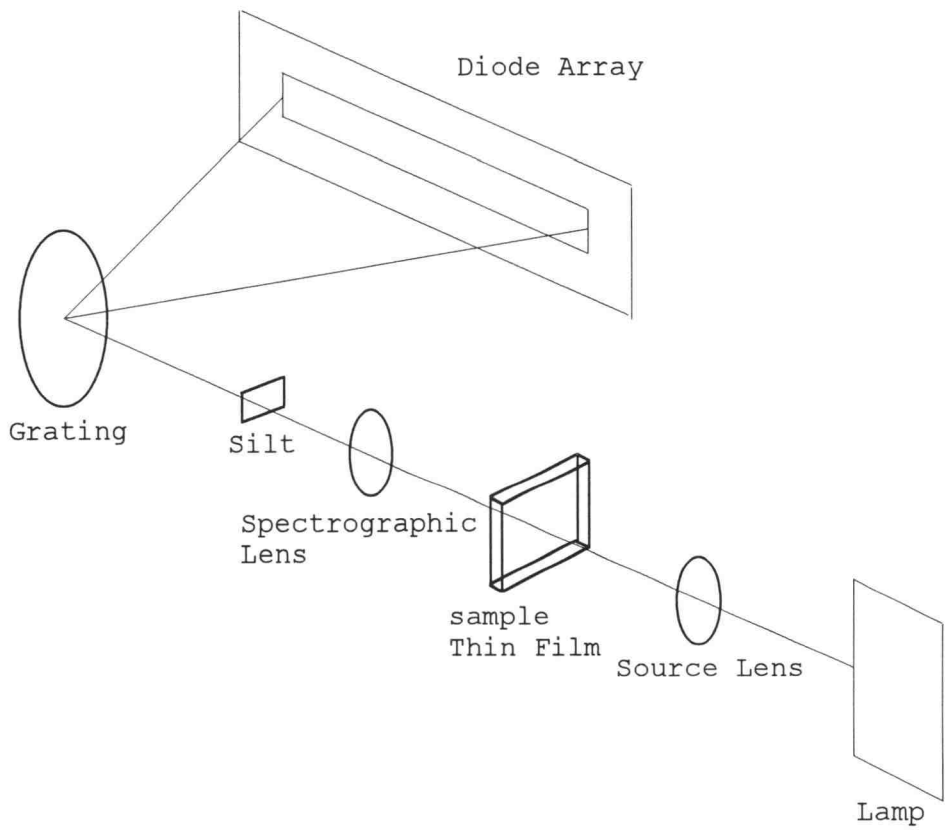

Fig. 3.7 Schematic diagram of a diode array spectrophotometer.

3.2.4 Resistivity and Breakdown Field Measurements

For resistivity and breakdown field measurements of PECVD-grown dielectric layers, a SiON film with a thickness of 1000 Å is deposited onto a silicon (Si) substrate. And 1000 Å thick aluminum (Al) dots with an area of about 11.06×10^{-3} cm^2 are formed on the top of the SiON film by thermal evaporation.

The resistivity of the SiON film is calculated from Ohm's law by measuring the current at a field of 1 MV/cm using a Hewlett-Packard (HP) 4240B pico-Ammerter with DC voltage source. The current is measured 60 seconds after applying the DC bias voltage in order to avoid transient effects. The resistivity, ρ, of the SiON layer is calculated from

$$\rho = \frac{A}{d}\frac{V}{I} \tag{3.6}$$

where A is the area, d is the thickness, V is the applied voltage, and I is the measured current flowing through the film.

The breakdown field is assessed from current-voltage (I-V) characteristics measured using a Hewlett-Packard 4145B Semiconductor Parameter Analyzer. From the I-V characteristic curve, a very small current increases linearly and slowly because of the very high resistivity of the SiON film. As soon as the electric field of the

dielectric layer exceeds the electric breakdown strength the current increases suddenly, and usually very sharp slope increase occurs due to the breakdown of the thin film. The breakdown voltage is defined as the voltage extrapolated from the I-V curve at the point where the slope of the current changes abruptly. The breakdown field is the breakdown voltage divided by the film thickness.

3.2.5 Characterization Techniques for ACTFEL Devices

The ACTFEL characterization techniques used in this thesis are capacitance-voltage (C-V)[38,76-78], internal charge-phosphor electric field (Q-F_p)[79,80], and luminance-voltage (L-V)[81] measurements. The experimental set-up for the C-V, and Q-F_p measurement is shown in Fig. 3.8. As shown, the ACTFEL device is connected in series with a series resistor (R_s), and a sense resistor (R_{sense}) for the C-V measurement or a sense capacitance (C_{sense}) for the Q-F_p measurement. R_s is used for the current limiting and helps to prevent the ACTFEL device from breaking down catastrophically. By measuring $v_1(t)$, $v_2(t)$, and $v_3(t)$, C-V and Q-F_p curves can be obtained.

When R_{sense} is used, the current through the sense resistor, $i(t)$, is written as

$$i(t) = \frac{v_3(t)}{R_{sense}} \quad . \tag{3.7}$$

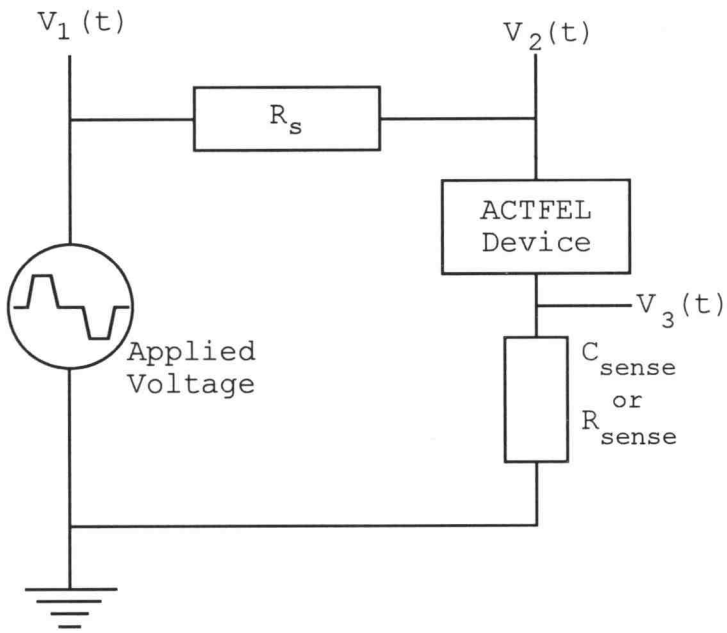

Fig. 3.8 Basic circuit for ACTFEL characterization.

By differentiating $q(t) = C\ v(t)$ with respect to time, the ACTFEL capacitance, C, as a function of the voltage across the ACTFEL device, v_2-v_3 can be described as

$$C(v_2 - v_3) = \frac{i(t)}{d[v_2(t) - v_3(t)] / dt} \quad . \tag{3.8}$$

C-V plot is then obtained by plotting $C(v_2-v_3)$ versus $v_2(t)-v_3(t)$.

If R_{sense} is replaced by C_{sense}, then , the internal charge, q(t), is written as

$$q(t) = \frac{C_I + C_p}{C_I} C_{sense} v_3(t) - C_p[v_2(t) - v_3(t)] \qquad (3.9)$$

where C_i and C_p are the insulator and phosphor capacitances of the ACTFEL device, respectively. The phosphor electric field, $F_p(t)$, can also be calculated as

$$F_p(t) = \frac{1}{d_p}\left[\frac{C_{sense} v_3(t)}{C_i} + \left(v_2(t) - v_3(t)\right)\right] \qquad (3.10)$$

where d_p is the thickness of phosphor layer of the ACTFEL device. By plotting q(t) versus $F_p(t)$, a Q-F_p curve is obtained.

The circuit used for L-V measurement is similar to that shown in Fig. 3.8 except that the ACTFEL device is operated without a sense resistor or capacitor. A photometer is placed in front of the ACTFEL device for measuring the luminance. By plotting the voltage across the ACTFEL device versus the luminance read from the photometer, a L-V curve is obtained.

From the C-V, Q-F_p, and L-V curves, valuable information about the ACTFEL device such as various threshold voltages, the insulator and phosphor capacitance, the interface charge density, the conduction charge, and the conversion efficiency, can be obtained; this is discussed in more detail in chapter 5.

Chapter 4. Inhomogeneous SiON Layers

4.1 Inhomogeneous SiON Layers Grown by PECVD

4.1.1 Generation of a Calibration Chart

Generation of a calibration chart is a first requirement for the fabrication of inhomogeneous dielectric layers. A large number of homogeneous SiON layers with different compositions are grown on Si substrates by varying the N_2O/N_2 flow rate ratio; then the refractive indices and thicknesses of these SiON films are measured by ellipsometry. A calibration chart is constructed by plotting the refractive indices and deposition rates as a function of the N_2O/N_2 flow rate ratio as shown in Fig. 4.1 (a) and (b), respectively. The

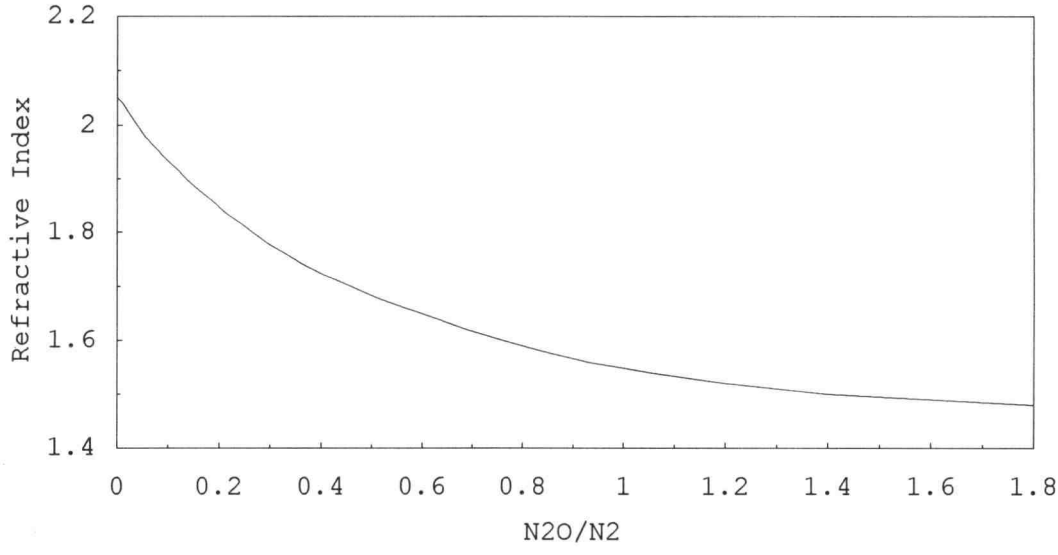

(a)

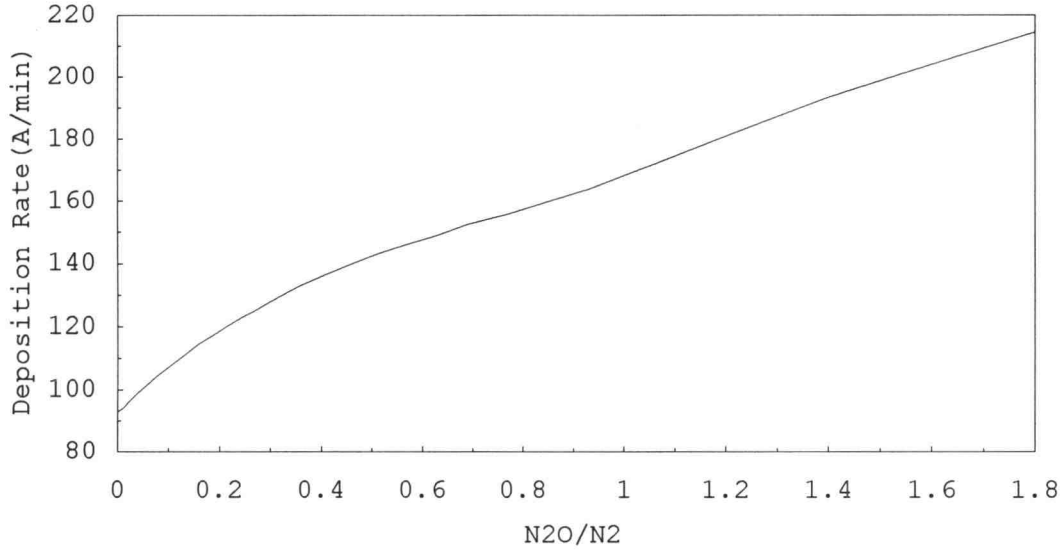

(b)

Fig. 4.1 SiON calibration chart. (a) Refractive index, and (b) deposition rate as a function of N_2O/N_2 flow rate ratio.

dynamic range of the index of refraction of a SiON layer varies from approximately 1.48 for SiO_2 to 2.05 for Si_3N_4. The minimum deposition rate of SiON films varies from about 93 Å/min. for Si_3N_4 growth to 214 Å/min. for SiO_2 growth. The flow rate ratios and deposition rates are selected according to the desired composition and thickness of the dielectric layer. The optical thin film is then synthesized by specifying the flow rate of the N_2O and the deposition time by writing a process control program using the PAL-68000 process automation system which controls the deposition in real-time.

4.1.2 Auger Electron Spectroscopy Analysis of Inhomogeneous Dielectric Layers

The results of Auger analysis of four dielectric layers grown by PECVD are shown in Figures. 4.2-4.5. Figs 4.2 and 4.3 are depth profiles of homogeneous SiO_2 and Si_3N_4 layers, respectively, deposited on silicon substrates. Note that the Si, O, and N atomic concentrations are almost constant as a function of sputtering time for these homogeneous layers.

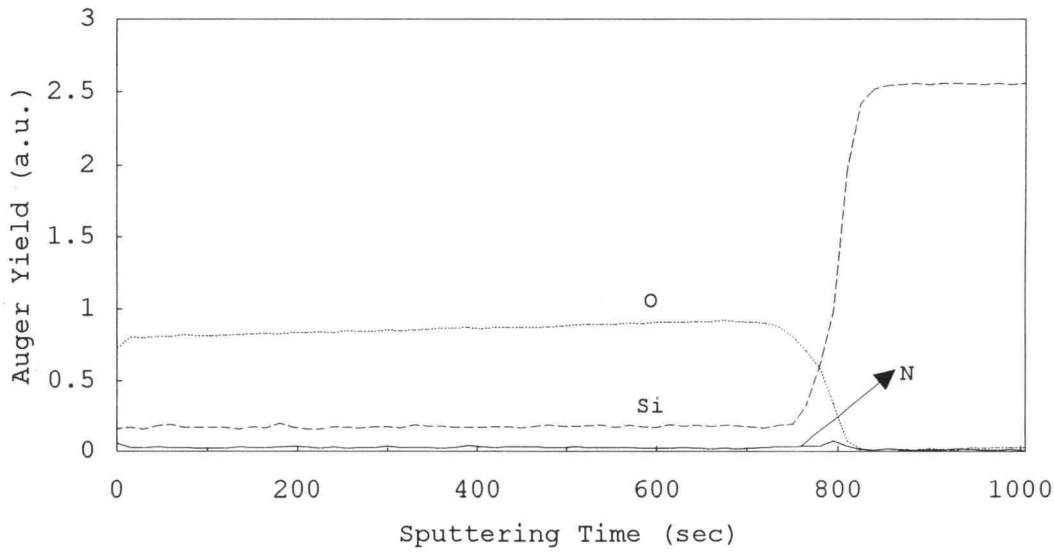

Fig. 4.2 Auger depth profile of a homogeneous SiO_2 layer.

Fig 4.4 displays the compositional variation of oxygen and nitrogen as a function of sputtering time for a linearly graded SiON layer. The depth profile shown in

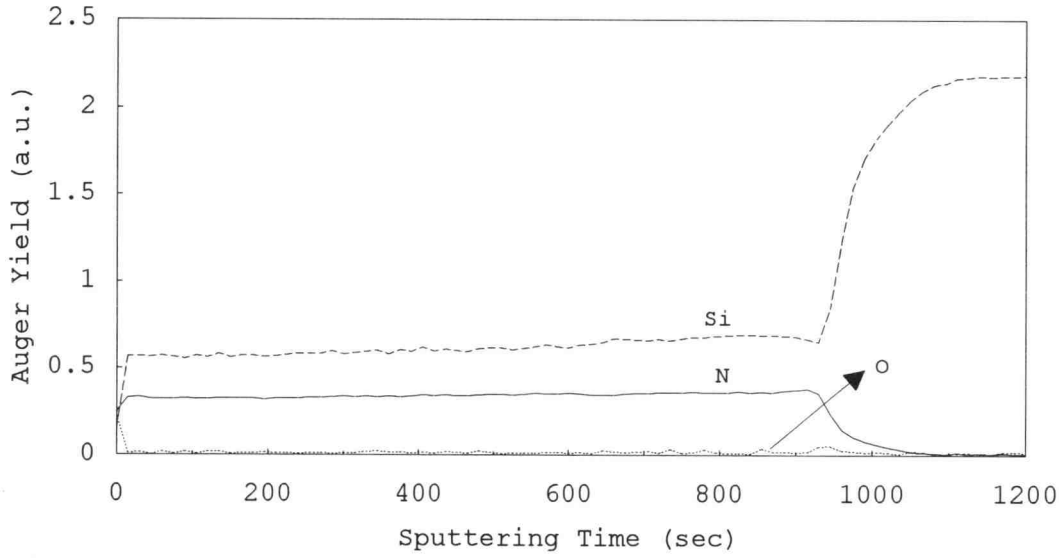

Fig. 4.3 Auger depth profile of a homogeneous SiN layer.

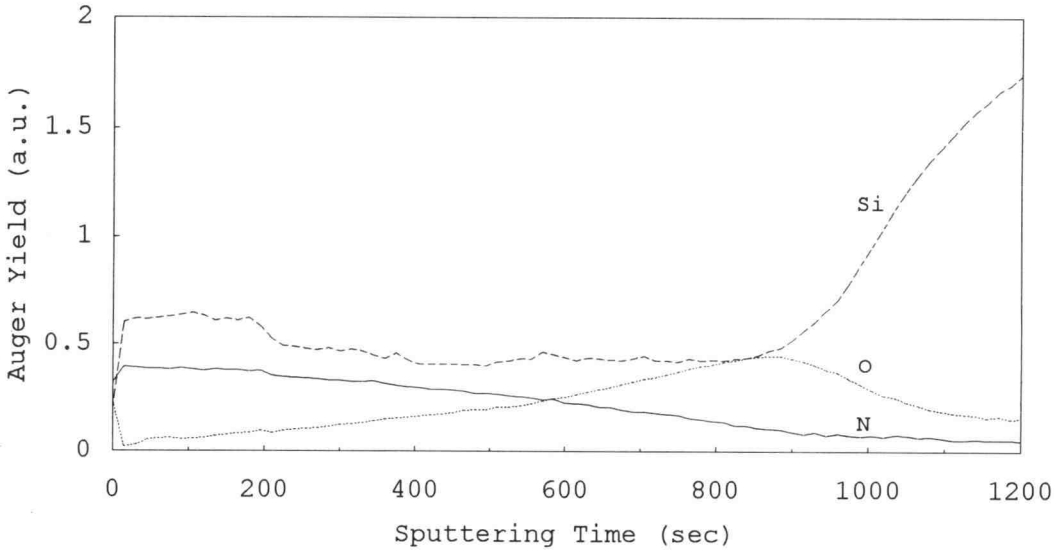

Fig. 4.4 Auger depth profile of an inhomogeneous SiON layer.

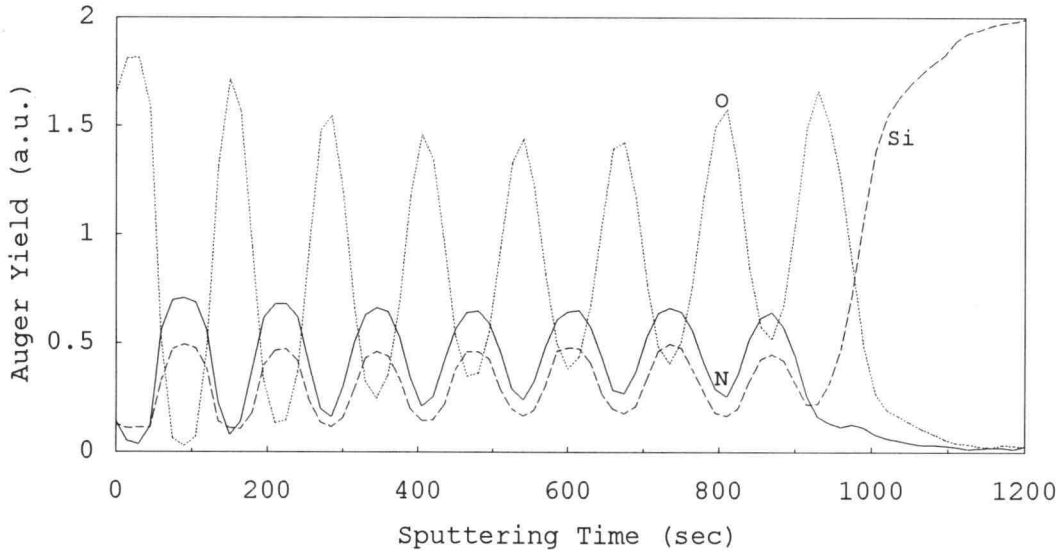

Fig. 4.5 Auger depth profile of a dielectric superlattice structure.

Fig. 4.5 is of a dielectric superlattice structure consisting of 8 SiO_2 and 7 Si_3N_4 layers. Much of the slow rise in the O and N signals found in Figs. 4.2 and 4.3 and the lack of abrupt interfaces observed in all four figures, as manifest by the rather long tails at interfaces, may be attributed to atomic remixing via knock-on effects associated with Ar^+ sputtering[74]. Thus, the Auger analysis results shown in Figs. 4.4 and 4.5 indicate that a high degree of compositional control has been achieved by computer-controlled PECVD growth of SiON layers.

4.1.3 Discussion

AES is used to analyze the homogeneous, compositionally graded, and superlattice-like SiON layers grown by computer-controlled PECVD by sputter profiling. It is demonstrated that the compositional variation of SiON thin films is possible by changing the gas flow rate using computer-controlled PECVD.

4.2 Antireflection (AR) Coatings

4.2.1 Transmission Line Modeling of a Thin Film

Transmission line theory can be used for the analysis of the propagation of electromagnetic waves in dielectric media. For example, a homogeneous dielectric layer grown on a glass substrate can be modeled as a transmission line with source and load impedances as shown in Fig. 4.6 , where l is

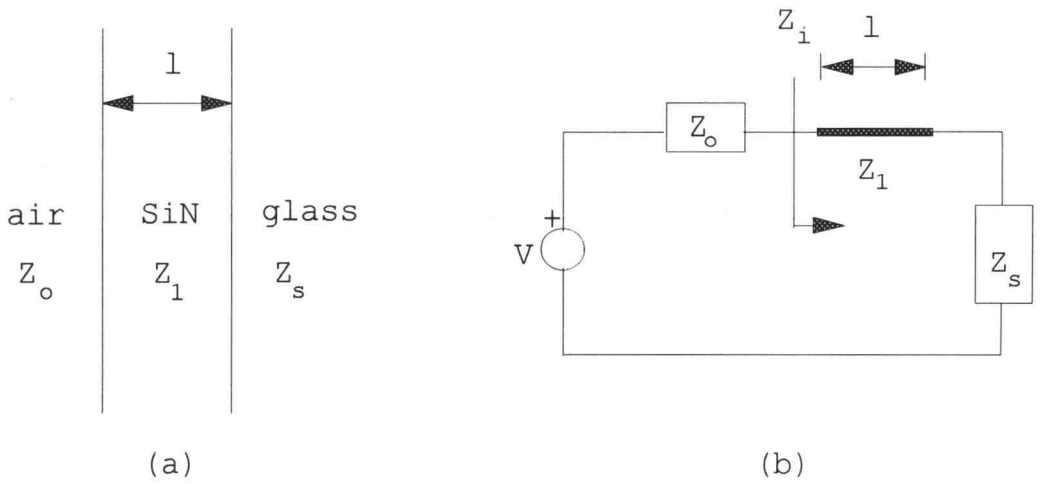

Fig. 4.6 (a) Air/SiN/glass structure and (b) its transmission line equivalent circuit.

the thickness of the dielectric layer, Z_o is the source impedance of free space, Z_s is the load impedance of the glass substrate, and Z_1 is the characteristic impedance of the SiN dielectric layer.

Assume that the dielectric layer is homogeneous, isotropic, and nonmagnetic; then the characteristic impedance Z_C is given by

$$Z_C = \sqrt{\frac{\mu\mu_o}{\varepsilon\varepsilon_o}} \tag{4.1}$$

where μ and μ_o are the relative permeability and the permeability of free space, respectively, and ε and ε_o are the relative permittivity of the dielectric material and permittivity of free space, respectively. The relative permeability, μ, is unity in non-magnetic dielectric materials. The relative permittivity, ε, or dielectric constant, differs from material to material. Therefore, different dielectric materials have different characteristic impedances. In free space, the dielectric constant, ε, is unity so that the characteristic impedance of free space, Z_o, becomes $Z_o=(\mu_o/\varepsilon_o)^{1/2}$. Thus, Z_C can be written as

$$Z_C = \sqrt{\frac{\mu_o}{\varepsilon_o}}\frac{1}{\sqrt{\varepsilon}} = Z_o\frac{1}{n} \tag{4.2}$$

where $n=\varepsilon^{1/2}$, and is denoted the refractive index of the dielectric material.

The reflection coefficient, r, at the interface of two semi-infinite materials with characteristic impedances of Z_1 and Z_2 is expressed by

$$r = \frac{Z_2 - Z_1}{Z_2 + Z_1} = \frac{n_1 - n_2}{n_1 + n_2} \tag{4.3}$$

where n_1 and n_2 are refractive indices of the two materials. From electromagnetics, the input impedance[82], Z_i, of a dielectric layer with thickness l with characteristic impedance of $Z_c = Z_1$, as shown in Fig. 4.6, is described as

$$Z_i = Z_1 \frac{Z_s + jZ_1 \tan \beta l}{Z_1 + jZ_s \tan \beta l} \tag{4.4}$$

where β, a propagation constant of the dielectric medium, is given by $\beta = \omega n/c$. Replacing Z_1 and Z_2 by Z_o and Z_i in Eqn. (4.3), it is possible to calculate the reflection coefficient at the surface of a film of thickness l on a glass substrate. Any multiple layer dielectric can be represented as a transmission line, as shown in Fig. 4.7. Therefore, the reflection coefficient of any multiple layer can be expressed in the same way; transmission line modeling

is useful for the analysis of multiple dielectric layer structures.

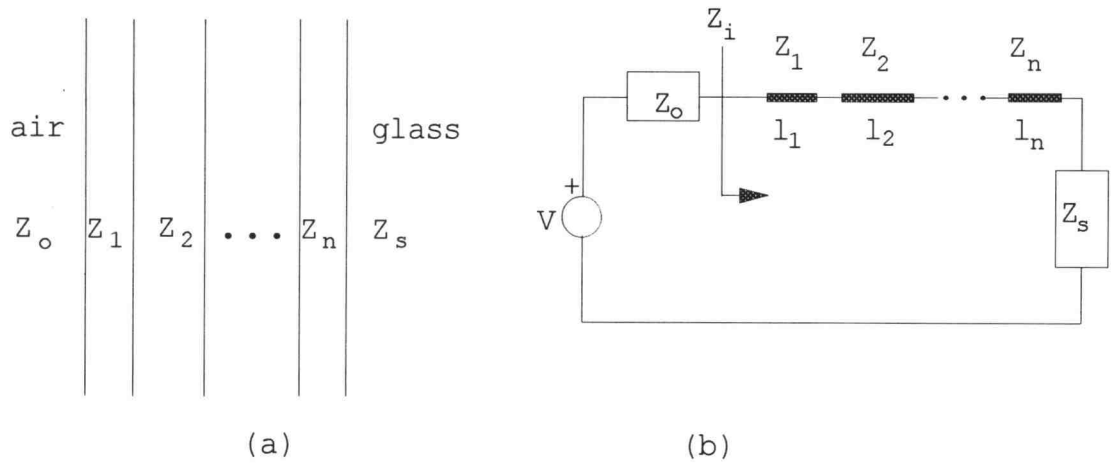

Fig. 4.7 (a) Multiple dielectric layer and (b) its transmission line equivalent circuit.

4.2.2 Touchstone Microwave Simulation and Optimization Program

Analysis of a multilayer dielectric film is quite straightforward if the multilayer structure is modeled as a transmission line structure shown in Fig. 4.7 as explained above. Synthesis of a multilayer structure, however, is a much more difficult problem than analysis. Young[28] applied a synthesis method in which multiple quarter-wave sections are used to design a multilayer AR coating with a desired spectral response. In order to simplify the synthesis problem he constrained the optical thickness to be the same

for each layer. Removal of this restriction allows the synthesis of a multilayer optical film with a spectral response closer to that of the desired specification.

Touchstone[83], developed by EEsof, is a microwave software program which can be used for the analysis and synthesis of transmission lines. No restrictions on the thickness and characteristic impedance are necessary using Touchstone and it can be directly applied to the analysis and design of AR coatings and impedance matching layers. An optimizing routine in the Touchstone makes the design of optimal multilayer dielectric films possible. The Touchstone optimizer first compares the computed transmission line circuit response with a desired response, and then adjusts the transmission line circuit parameter values (thickness and impedance or refractive index) to minimize the difference between the computed and desired responses. The subsequent analysis and design of AR coatings are calculated by the Touchstone.

4.2.3 Analysis and Optimization of AR Coatings

An ideal AR coating has a gradually changing refractive index profile between the incident medium and exit medium in order to transmit 100% power to the exit medium. However, the gradual change of refractive index from air (n=1) to glass substrate (n=1.52) is not possible because of refractive index limitations. The minimum refractive index

of a dielectric material such as MgF_2 in the visible frequency range is 1.38. The minimum refractive index of a SiON film grown by PECVD is 1.48. An ideal, single layer AR coating has an index of refraction, n, related to that of the glass substrate, 1.52, and air, 1, by $n=(1\times1.52)^{1/2}=1.23$; however, there is no suitable coating material available. By placing a quaterwave-thick homogenous dielectric layer with a high refractive index between air and a linearly graded inhomogeneous dielectric layer on a glass substrate it is possible to reduce the reflectance over the design wavelength. A first-cut design of the refractive index profile is shown in Figs. 4.8.

In order to calculate the spectral response of such a linearly graded AC coating using Touchstone, it should be

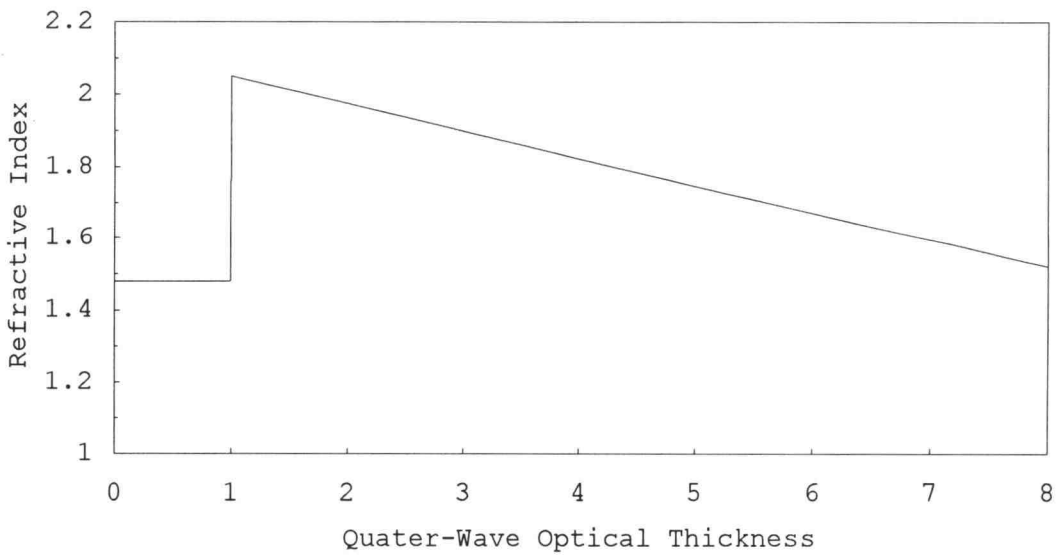

Fig. 4.8 Refractive index profile of a linearly graded AR coating on a glass substrate.

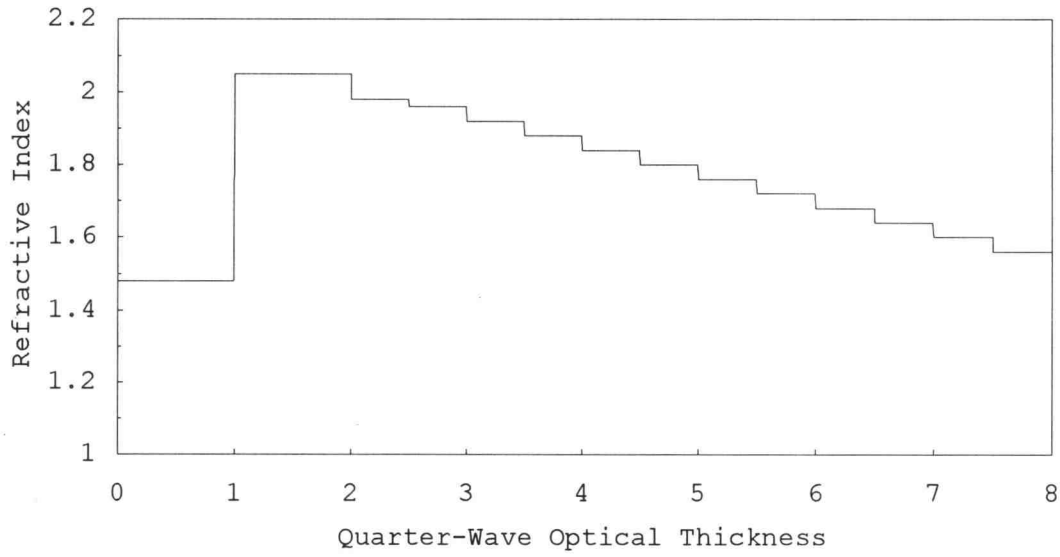

(a)

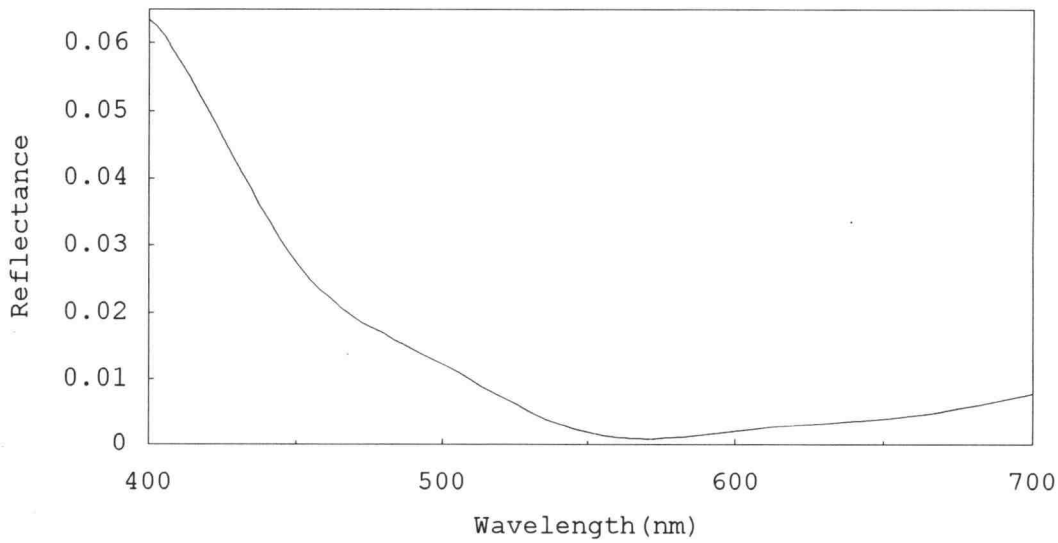

(b)

Fig. 4.9 (a) Discretization of the linearly graded AR coating in Fig. 4.8, and (b) calculated reflectance response of the discretized structure in (a).

divided into a thin multiple layer structure as shown in Fig. 4.9 (a) which can be represented as a transmission line. It is divided into 14 layers for convenience. (For the transmission line analysis using the Touchstone, an AR coating can be divided into as many as 2500 layers. But the maximum number of layers the Touchstone optimizer can handle is limited to 25.) The spectral response, thus calculated, is shown Fig. 4.9 (b). The Touchstone optimizer is used to find the optimum design parameters and the resulting design and its reflectance spectrum is shown in Figs. 4.10 (a) and (b). From a comparison of the spectral response of the two structures in Figs 4.9 (b) and 4.10 (b), the latter shows better spectral response in the visible range.

4.2.4 Experimental Results of AR Coatings

Fourteen layers of SiON thin films, as shown in Fig. 4.10 (a), are deposited on a Corning 7059 glass substrate (n = 1.52) by computer-controlled PECVD. The total thickness of the AR coating is approximately 1000 nm. The measured spectral response of the multiple layer AR coating is indicated in Fig. 4.10 (b), shows good agreement with the simulated result.

Even though the dynamic range of the refractive index of SiON films grown by PECVD is limited from 1.48 to 2.05, a reflectance of less than 0.5% over the visible wavelength

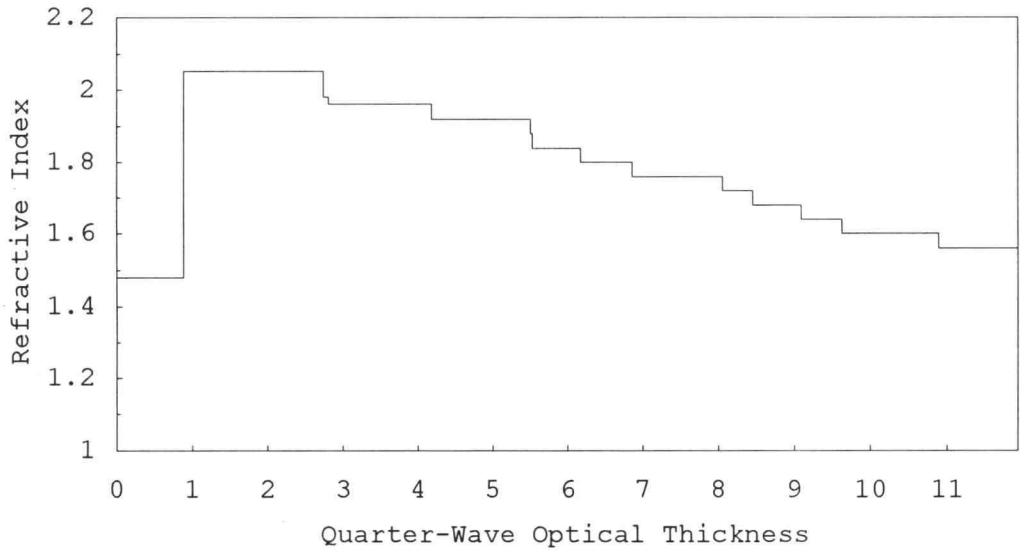

(a)

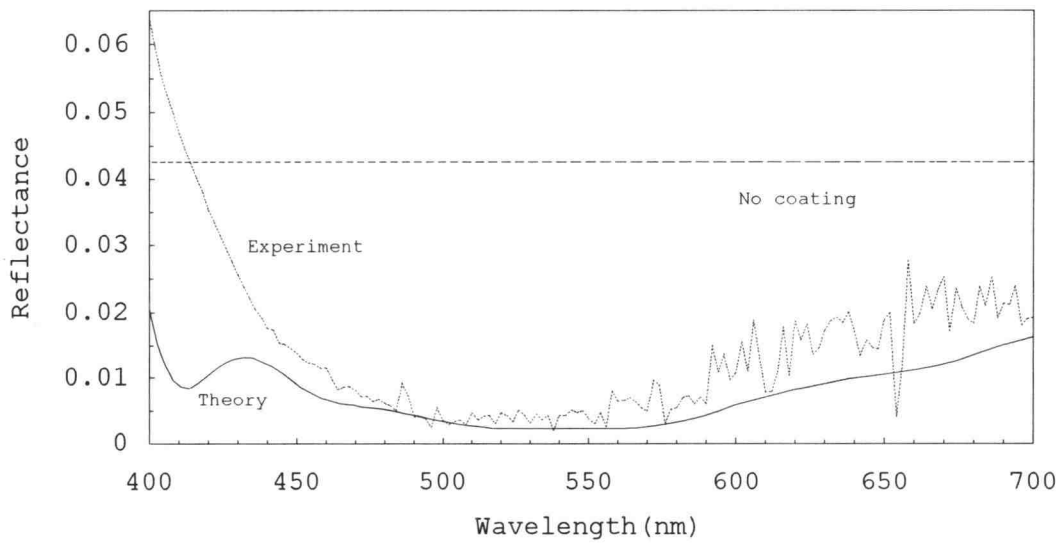

(b)

Fig. 4.10 Multilayer AR coating structure on a glass substrate (n_s=1.52): (a) refractive index profile, (b) spectral response of calculated and measured AR coatings. The straight line shows the glass reflectance without a coating.

range is realized by the deposition of 14 SiON layers on a glass substrate.

4.3 Rugate Filters

4.3.1 Design of Rugate Filters

Using the analytical solution described in Chapter 2, two rugate filters with bandwidths of around 100 nm at central wavelengths of 500 nm and 570 nm are designed. The design parameters Λ and n_1 can be calculated from the equations derived in Chapter 2.

From Eqns. (2.24), (2.27), and (2.29), Λ can be written as

$$\Lambda = \frac{\lambda_o}{2n_o} \tag{4.5}$$

where Λ is the thickness of a period of the sinusoidal layer, λ_o is the central wavelength, and n_o is the average refractive index of the rugate filter. The amplitude of modulation, n_1, is derived from Eqn. (2.43) and is given by

$$n_1 = \frac{n_o}{2}\left|\frac{\Delta\lambda}{\lambda_o}\right| . \tag{4.6}$$

A rugate filter with a central wavelength λ_o = 500 nm and a bandwidth $\Delta\lambda$ = 100 nm is designed using Eqns. (4.5) and (4.6). An average value of refractive index n_o = 1.66 is

chosen as a quiescent point for the full swing of the sinusoidal refractive index. (It is not easy to control the N_2O flow rate for a SiON film with high refractive index because the MFC cannot control the N_2O flow rate in a range less than 2 % of the maximum flow rate; the lower the N_2O flow rate is , the higher the refractive index of a SiON film grown by a computer-controlled PECVD.) The calculated values of Λ and n_1 are 150.6 nm and 0.166, respectively. Another rugate filter with central wavelength λ_o of 570 nm is designed. The average index of refraction, n_o, and the amplitude of modulation, n_1, are chosen to be the same as those of the λ_o = 500 nm rugate filter. The calculated values of Λ and $\Delta\lambda$ are Λ = 171.6 nm and $\Delta\lambda$ = 114 nm, respectively for this case. The specification of the two rugate filters, including the number of sinusoidal periods to be grown, is shown in Table 4.1. Theoretically calculated reflectance spectra of the two rugate filters are shown in Figs. 4.11 and 4.12. These spectra are calculated using the matrix method.

4.3.2 Experimental Results

Rugate filters with 10 and 20 sinusoidal periods are fabricated by computer-controlled PECVD. The measured spectral characteristics of 10 and 20 sinusoidal period rugate filters are compared to simulated results and are shown in Figs. 4.11 and 4.12, respectively.

Table 4.1 Parameters of rugate filters fabricated by computer-controlled PECVD.

	λ_o	Λ	n_o	n_1	$\Delta\lambda$	# of periods
Rugate Filter #1	500 nm	150.6nm	1.66	0.166	100 nm	10
Rugate Filter #2	570 nm	171.6nm	1.66	0.166	114 nm	20

It took approximately two hours to grow the 10 sinusoidal periods on a glass substrate. The thickness is approximately 1.5 μm for the 10 sinusoidal period rugate filter. Compared to the 107 hours of deposition time taken to grow a 30 μm thick rugate filter by Oullette et al.[13], it would take less than 30 hours to grow a rugate filter with the same characteristics by PECVD. Figure 4.11 displays good agreement between the theoretical simulation and the experimental assessment of the two rugate filters grown under the identical conditions. Note that the experimental spectra are quite similar; this is indicative of the reproducibility of the present PECVD process.

It took approximately four hours to grow a 20 sinusoidal period rugate filter on a glass substrate. The thickness is approximately 3.4 μm for the 20 sinusoidal

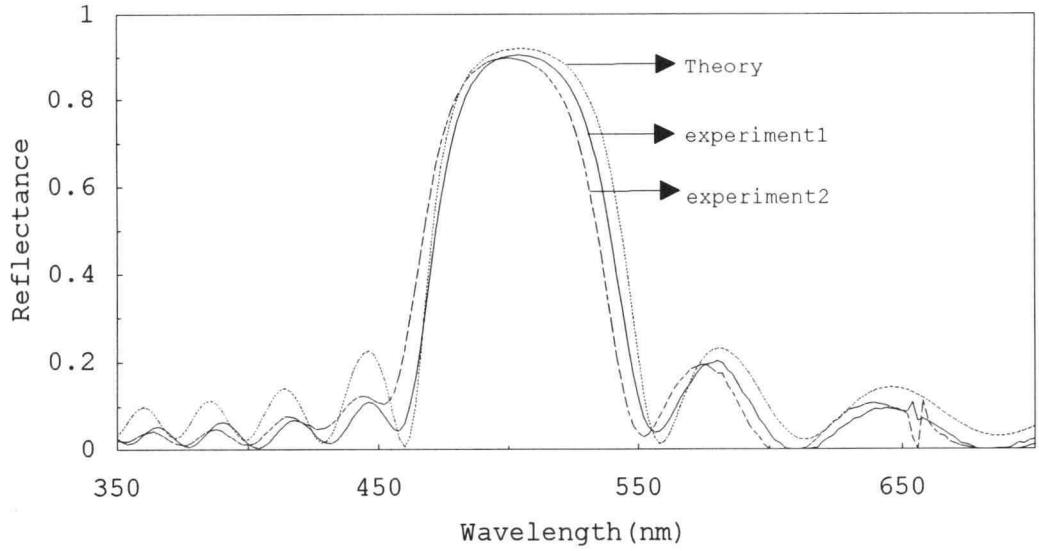

Fig. 4.11 Theoretical and experimental reflectance spectra for 10 sinusoidal period rugate filters on a glass substrate with λ_o = 500 nm.

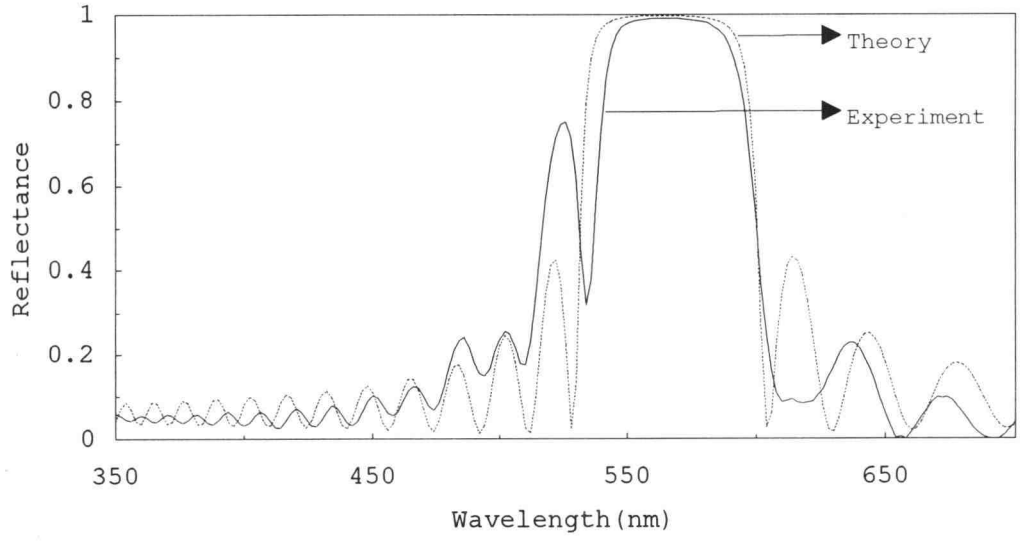

Fig. 4.12 Theoretical and experimental reflectance spectra for a 20 sinusoidal period rugate filter on a glass substrate with λ_o = 570 nm.

period rugate filter. The measured spectral response of the rugate filter with 20 sinusoidal periods varied from point to point due to the nonuniformity of the thickness of the film. (The present PECVD process has not been optimized for thickness uniformity.) The spectral response shown in Fig. 4.12 is chosen because it is most similar to the simulated spectra. The main deviation between the experimental and simulated spectra of Fig. 4.12 for the 20 period rugate filter is with respect to differences in the sidelobes.

In order to investigate possible sources of the origin of differences between the simulated and experimental sidelobes, a sensitivity analysis is undertaken in which several reflectance spectra are generated as a function of variations in the refractive index profile. For example, Fig. 4.13 shows reflectance spectra in which n_o and n_1 are increased by 5 % compared to that of an original design. Note that a 5 % variation in n_1 changes the spectral response insignificantly whereas a 5 % variation in n_o changes the central wavelength of the filter dramatically. Fig. 4.14 illustrates that a 5 % increase in Λ yields a large change in the central wavelength of the filter and that the number of layers determine the steepness of the band edge rejection transition. However, note the none of the variations

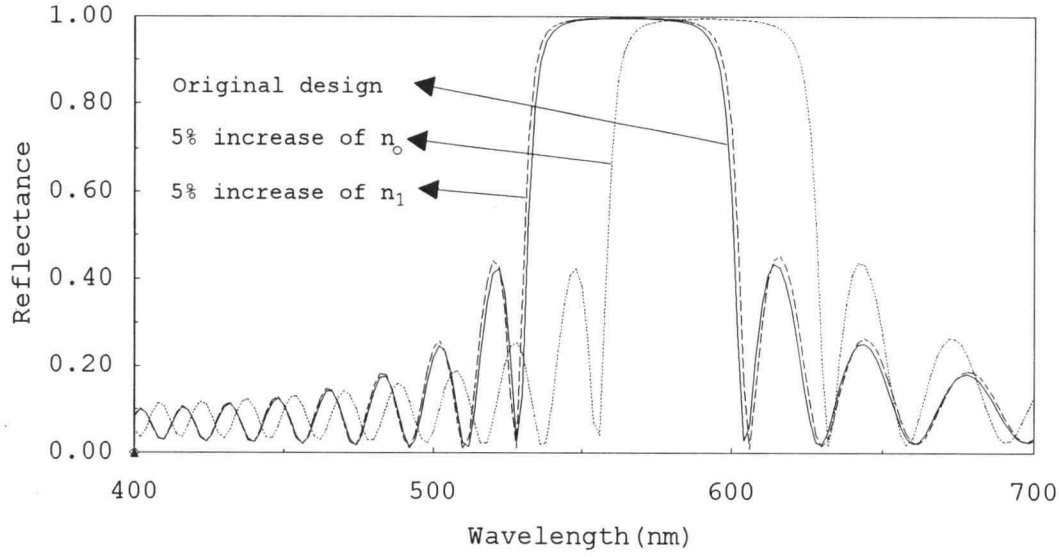

Fig. 4.13 Reflectance spectra of a rugate filter due to the variation of n_o and n_1.

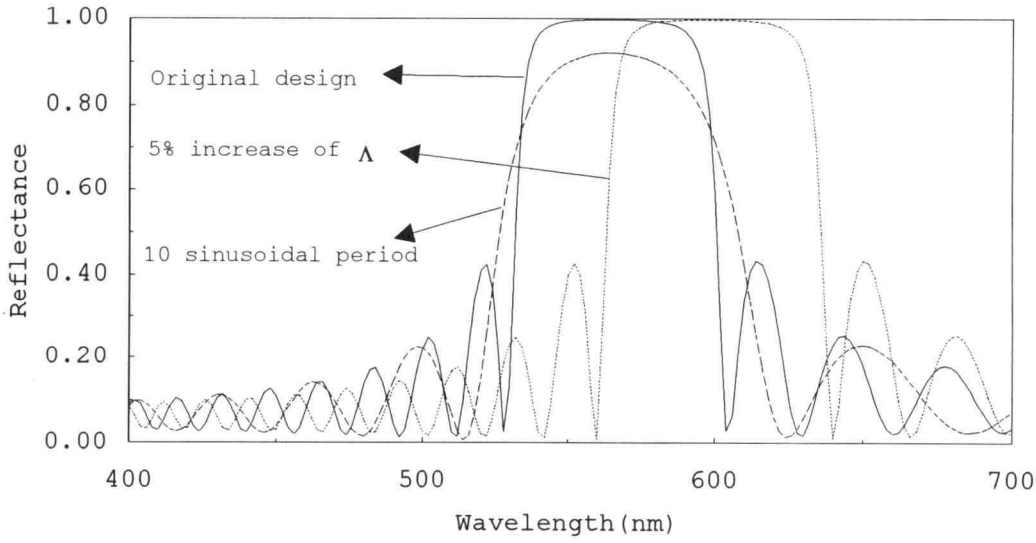

Fig. 4. 14 Reflectance spectra of a 20 period rugate filter due to the variation of Λ and the number of sinusoidal periods.

considered in Figs. 4.13 or 4.14 can allow for the sidelobe deviations encountered in Fig. 4.12.

The variation of spectral response a 20 period rugate filter is investigated on the assumption that phase shift may occur in the refractive index profile; i.e. the thickness of the rugate filter is a non-integral number of periods. The refractive index of a rugate filter as a function of position and phase is given by

$$n(z) = n_o + n_1 \sin(\frac{2\pi}{\Lambda} z + \phi) \qquad (4.7)$$

where ϕ is the phase, the value of which may be process-dependent. ϕ is assumed zero in the original design and simulation. The simulated spectral response for ϕ = 0, $\pi/4$,

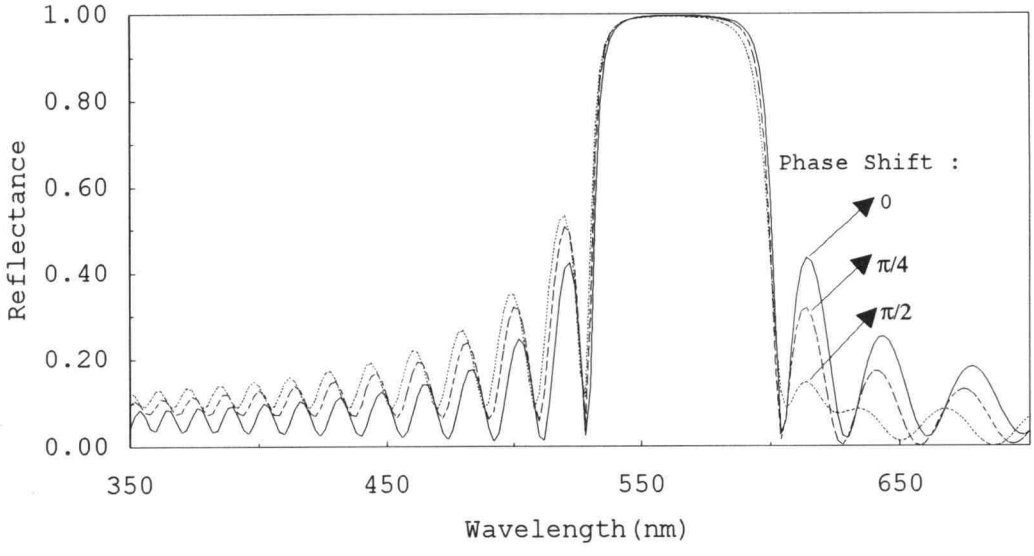

Fig. 4.15 Reflectance spectra of a 20 period rugate filter as a function of phase shift.

and $\pi/2$ is shown in Fig. 4.15. Fig. 4.15 shows changes in the sidelobes as a function of phase. When $\phi = 0$, the magnitude of the amplitudes of the sidelobes in the long- and short-wavelength regions is very similar. However, as ϕ increases to $\pi/2$, the sidelobe amplitude in the short-wavelength region is more pronounced than that in the long-wavelength region. In Fig. 4.16, the simulated spectral response at $\phi = \pi/2$ is compared with experiment. This simulation is more in keeping with the sidelobe structure observed for the rugate filter of Fig. 4.12. Thus, the phase shift of the refractive index profile is one of the major sources which can account for the

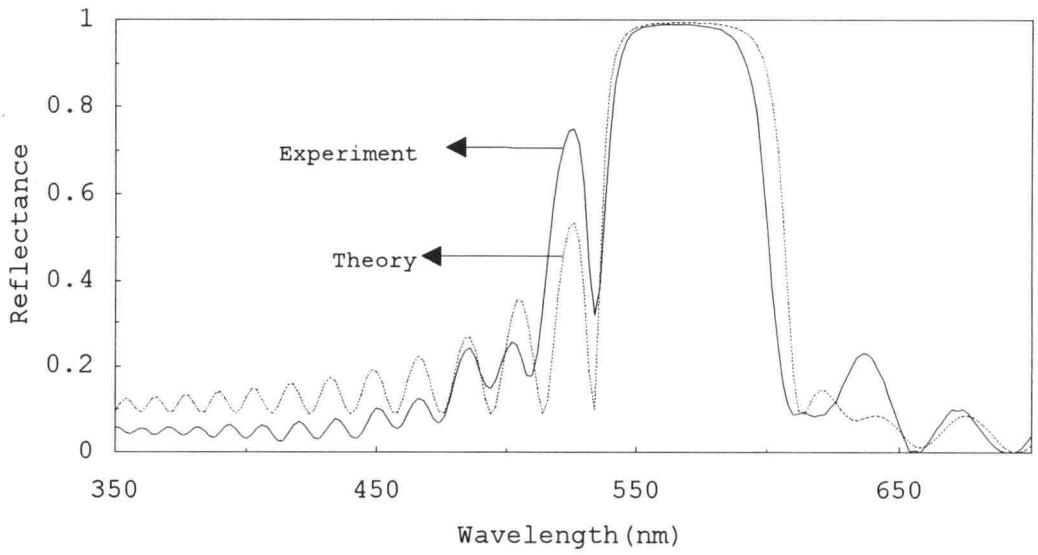

Fig. 4.16 Simulated spectral response of a 20 layer rugate filter with a phase shift of $\pi/2$ compared to the experimental spectrum.

sidelobe disagreement observed in Fig. 4.12.

The physical mechanism responsible for the phase shift of the refractive index profile may be changes in the refractive index of SiON film at air/SiON/glass interface due to a contamination (due to oxidation, for example) or simply due to the nonuniform thickness of the film which appears to manifest itself as a phase shift[96]; further work is required to establish this conclusively. Sensitivity analysis, such as that demonstrated in the preceding, is a valuable approach for establishing the limits of design sensitivity for rugate filters.

Another possible source of deviation between the experimental and simulated spectra for the 20 sinusoidal period rugate filter is likely to be tiny particulates which have fallen onto the substrate from the surface of the top electrode during the long period of deposition; there is a large number of tiny particulates on the surface of the 20 period rugate filter, as observed under the microscope. This is an ever-present problem for horizontal chamber configurations[96]. These particles cause scattering of the light which can also give rise to deviations from the simulated spectra.

4.3.3 Summary

10 and 20 sinusoidal period rugate filters are realized on glass substrates. Excellent agreement between the measured and simulated spectral responses of 10 sinusoidal period rugate filters demonstrates the effectiveness of computer-controlled PECVD for the growth of inhomogeneous SiON dielectric layers.

The deviation of the sidelobes of the measured spectral response of the 20 sinusoidal period rugate filter may be attributed to the phase shift of the refractive index profile of the rugate filter. It is likely that the phase shift of the refractive index profile is due to changes in the refractive index at the air/SiON or SiON/glass interface or due to the nonuniform thickness of the film, but further investigation is needed to prove this. Thickness nonuniformities and problems with particulates may be resolved by employing a reactor in which the substrate temperature is maintained constant and the substrates sit vertically.

Chapter 5. ACTFEL Devices with Inhomogeneous Dielectrics

5.1 Design of ACTFEL Devices with SiON Dielectric Layers

5.1.1 The Role of Insulating Layers in ACTFEL Devices

A conventional ACTFEL device structure (metal electrode/first insulator/phosphor layer/second insulator /indium tinoxide (ITO)/glass) is shown in Fig. 5.1. When an external voltage is applied between the metal and ITO

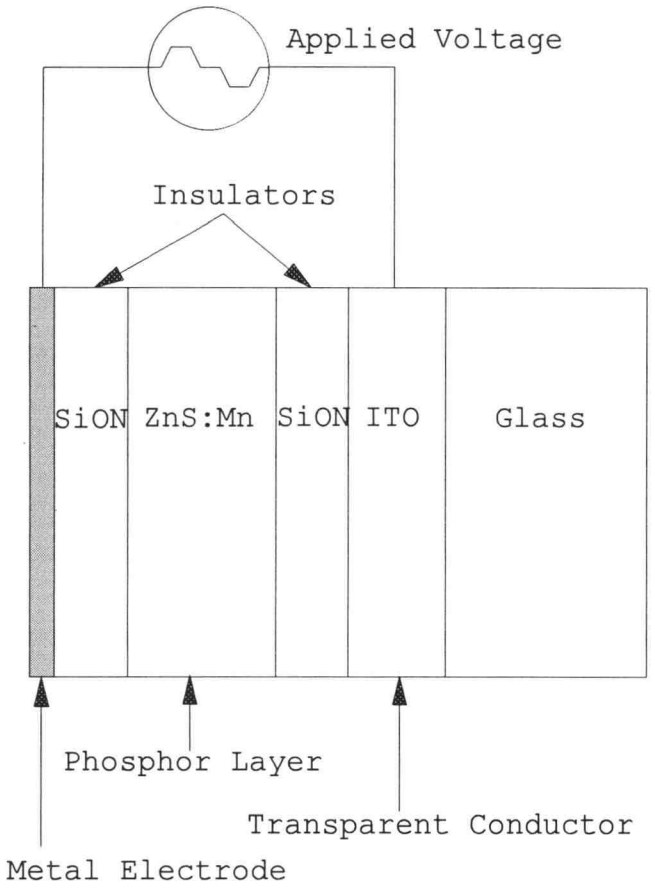

Fig. 5.1 Structure of a conventional ACTFEL device.

electrode, light is generated in the phosphor layer and is transmitted through the insulator, ITO, and glass substrate. The role of the dielectric layer in an ACTFEL device is to prevent catastrophic breakdown by the flow of DC current and, thus, to secure the stability of the device, to confine electrical conduction to the phosphor layer, and to prevent moisture from penetrating into the phosphor layer. The ACTFEL device is operated at very high electric fields of greater than 1 MV/cm so that the dielectric layer must have a high dielectric breakdown strength; it also needs to satisfy mechanical strength requirements. A frequently used material for ACTFEL dielectric layers is SiON films deposited by sputtering.

An ACTFEL device can also be considered as an optical interference filter because it is composed of several layers of thin films with thicknesses comparable to that of the wavelength of light. The thicknesses of the ITO and phosphor layers are fixed for production convenience. Therefore, it may be possible to adjust the dielectric layer thicknesses to achieve maximum light output from the ACTFEL device. A single, homogeneous dielectric layer on both sides of the phosphor layer is the conventional ACTFEL structure. The purpose of this portion of the thesis is to attempt to improve the efficiency of an ACTFEL device by using a multiple layer insulating structure for maximum optical transmittance through the

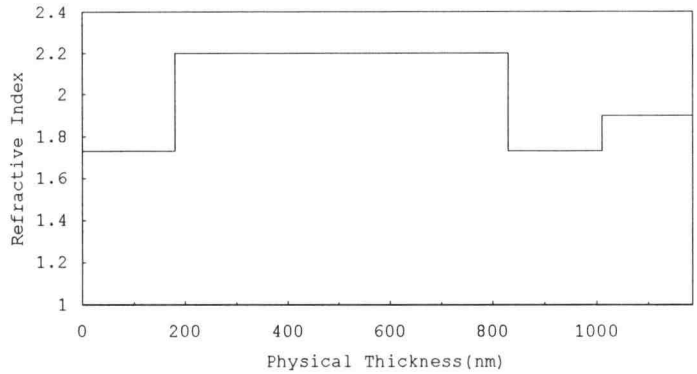

(a)

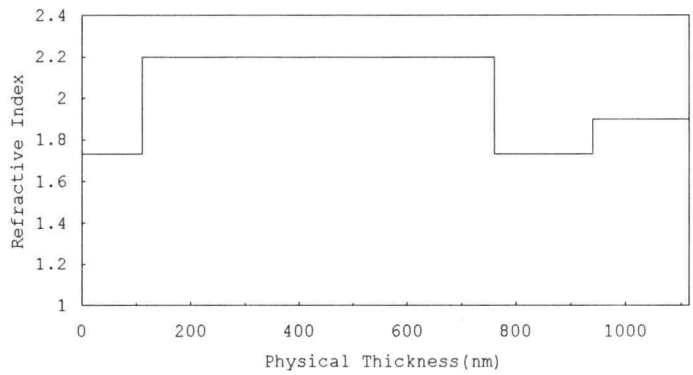

(b)

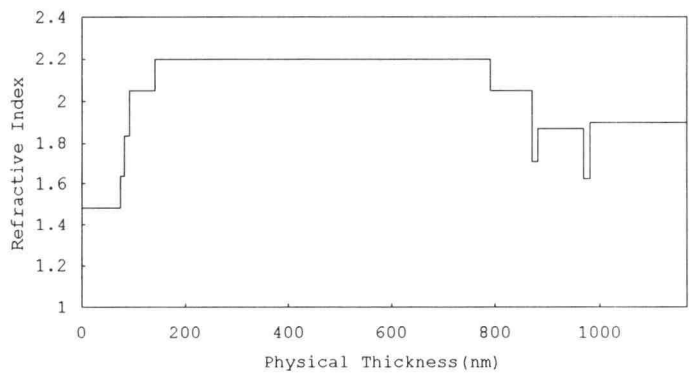

(c)

Fig. 5.2 ACTFEL device refractive index profiles for (a) a conventional single-layer dielectric structure previously used by Planar Systems, (b) a conventional single-layer dielectric structure used currently by Planar Systems, and (c) a multiple dielectric layer structure optimized for maximum transmittance of light through the entire stack.

device.

5.1.2 Design of Dielectric Layers in ACTFEL Devices

In this chapter multiple dielectric layer structures are employed as the first and second insulating layers. It is assumed that external light is incident on the ACTFEL device from the Al electrode side (without the Al metal present) in Fig. 5.1 and is transmitted to the right. The insulating layers are divided into 8 homogeneous SiON layers with different refractive indices. Using the transmission line equivalent circuit approach discussed in Chapter 4, the spectral response of an ACTFEL device is calculated. The Touchstone optimizer is used to obtain optimized parameters for the maximum transmittance. The thicknesses and indices of refraction are chosen to have the optimum optical transmittance in an attempt to increase the optical efficiency of an ACTFEL device.

Two conventional ZnS:Mn ACTFEL structures with different dielectric layer thicknesses which have been used by Planar System for production are selected as references. The refractive index profile for the two conventional ACTFEL structures and for one multiple layer SiON ACTFEL structure are shown in Figs. 5.2. Figures 5.2 (a) and (b) are Planar's old and new ACTFEL structures, respectively. The refractive index profile for the ACTFEL device, optimized for maximum optical transmittance, is shown in Fig. 5.2 (c). The three

samples shown in Fig. 5.2 are referred to as samples a, b, and c throughout the remainder of this chapter. The calculated transmittance spectra in the visible range for the three structures shown in Fig. 5.2 is given in Fig. 5.3. From Fig. 5.3 it is shown that the transmittance of the multiple dielectric layer structure is the highest at λ_o = 585 nm, as well as over most of the visible spectrum.

5.2 Experimental Results

Three ACTFEL devices, whose structures are shown in Figs. 5.2 (a), (b), and (c), are fabricated. Dielectric layers are grown on a Corning 7059 glass substrate. Because the cleanliness of the substrate is very important, the 7059 substrates are ultrasonically cleaned in DI water, methanol, and DI water for 5 min. each, and then blown dry with nitrogen. After the bottom dielectric layers were grown by computer-controlled PECVD, they were placed in a vacuum desiccator and sent to Planar Systems for deposition of the ZnS:Mn phosphor layer. After the phosphor layer deposition, all samples were annealed for one hour at 460°C. They were then placed in the vacuum desiccator and returned to OSU where the top dielectric layers were grown by computer-controlled PECVD. Finally, 1000Å thick Al electrodes were deposited by vacuum evaporation. From L-V, C-V, and Q-F_p measurement, several ACTFEL parameters are deduced to calculate the ACTFEL

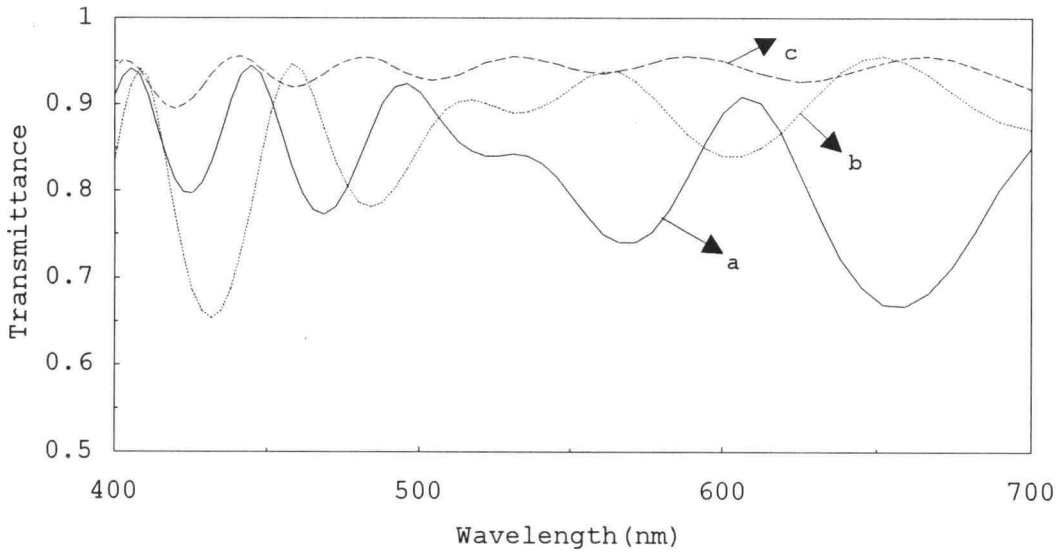

Fig. 5.3 Calculated spectral responses of ACTFEL devices a, b and c shown in Fig. 5.2.

efficiency and are compared to the measured transmittance characteristics.

5.2.1 Optical Transmittance

The optical transmittances T_a, T_b, and T_c of samples a, b, and c as a function of wavelength are measured in the visible range and are shown in Fig. 5.4. Over most of the visible spectrum the trend is $T_c > T_b > T_a$. Note that the measured transmittance spectra of these three samples a, b, and c differs from those calculated and shown in Fig. 5.3. These differences are possibly due to deviations of the refractive index and thickness of the multiple SiON, ZnS, or ITO layers from that of their target values. Alternatively, it is possible that the 460°C anneal for one

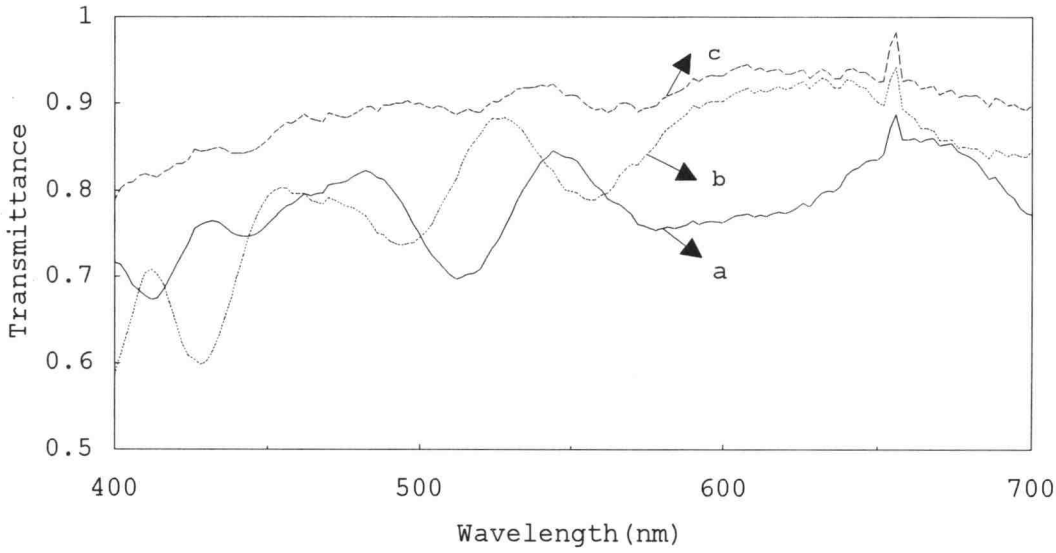

Fig. 5.4 Measured transmittance spectra of samples a, b, and c.

hour could be responsible for the differences between the calculated and measured transmittance spectra since the anneal could presumably lead to changes in the indices of refraction of the stack of ACTFEL materials due to interdiffusion, hydrogenation, evaporation, etc.; more work is necessary to resolve the details responsible for deviations between the simulated and experimental spectra. Even though there are differences between the calculated and measured transmittance spectra, the transmittance spectra trend is the same for both sets of spectra.

5.2.2 Luminance-Voltage (L-V) Characteristics

Figure 5.5 shows the L-V characteristics of the three

samples a, b, and c. The frequency of the applied waveform is 1 KHz and the voltage waveform has a 30 μsec duration at the maximum voltage. The threshold voltage, V_{th}, shown in Fig. 5.5 for sample a, is one of the important parameters for assessing the ACTFEL efficiency. From Fig.

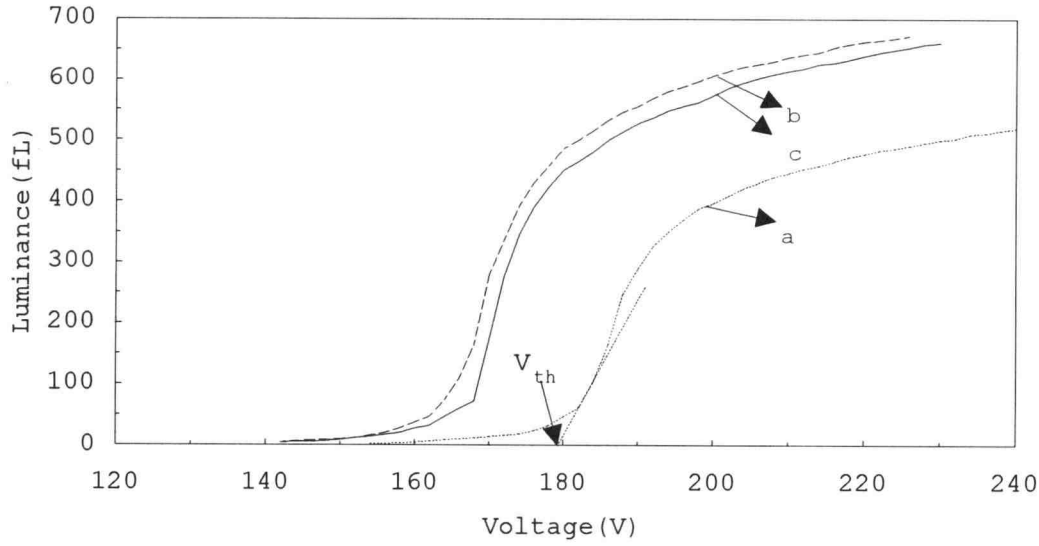

Fig. 5.5 L-V characteristics for samples a, b, and c.

5.5, the threshold voltages for samples a, b, and c are 179 V, 162 V, and 164 V, respectively. The differences of the threshold voltages are due to the differences of insulating layer thicknesses. Also the luminance is one of the important ACTFEL parameters for assessing ACTFEL efficiency; the luminances measured at 40 V above the threshold voltage are 480 fL, 635 fL, and 606 fL for samples a, b, and c, respectively.

5.2.3. Capacitance-Voltage (C-V) Characteristics

Figure 5.6 shows the C-V curves of samples a, b, and c. The insulator capacitance, C_i, and the total capacitance, C_t, which is a series combination of C_i and phosphor capacitance, C_p, can be estimated from the C-V curve shown in Fig. 5.6. Using the C_i and C_p values

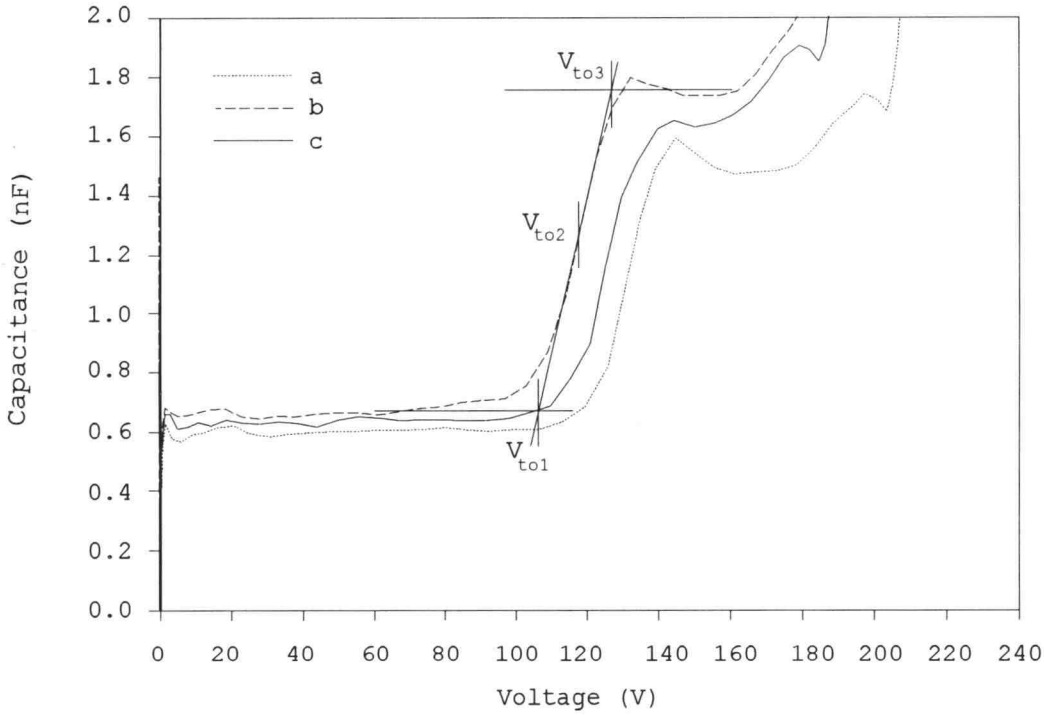

Fig. 5.6 C-V characteristics of ACTFEL devices a, b, and c.

obtained from Fig. 5.6, the phosphor threshold voltage can be calculated. C_i and C_p are important parameters for constructing a Q-F_p curve. The values for C_i, C_p, and C_t are

collected in Table 5.1, along with various other parameters discussed in the following.

The turn-on voltage, V_{to1}, at which electrons in shallow interface traps at the phosphor-insulator interface start being emitted, the mid-point turn-on voltage, V_{to2}, which corresponds to the turn-on voltage measured in charge-voltage (Q-V) analysis, and the upper turn-on voltage, V_{to3}, at which field-clamping occurs, are found as shown in Fig. 5.5. These values are useful for the estimation of the interface state density at the phosphor/insulator interface. The slopes $\frac{C_i - C_t}{V_{to3} - V_{to1}} = \frac{\Delta C}{\Delta V}$ of the C-V curves in Fig. 5.5 in the transition region, are found to be almost the same for all three ACTFEL devices; this implies that the interface state density is relatively constant and independent of which dielectric material is adjacent to the phosphor. The interface state density is obtained as[76,77]

$$Q_{ss} = \frac{C_i^2}{2qA} \frac{C_t}{C_p} [\frac{\Delta C}{\Delta V}]^{-1} \quad . \tag{5.1}$$

5.2.4 Charge-Phosphor Field ($Q-F_p$) Characteristics

Figure 5.7 shows the $Q-F_p$ characteristics for samples a, b, and c. Various ACTFEL device physics parameters are assessed from these $Q-F_p$ curves obtained at 40V above the turn-on voltage and are tabulated in Table 5.2. The

Table 5.1 ACTFEL device parameters deduced from C-V characteristics.

		ACTFEL a	ACTFEL b	ACTFEL c
V_{to1}	[V]	123	107	115
V_{to3}	[V]	139	127	135
V_{to2}	[V]	131	117	125
C_i	[nF]	1.5	1.75	1.65
C_p	[nF]	1.0	1.034	0.993
C_t	[nF]	0.6	0.65	0.62
Q_{ss}	[/cm^2]	4.75×10^{11}	6.92×10^{11}	6.53×10^{11}
$\Delta C/\Delta V$	[nF/V]	0.056	0.057	0.052

conduction charge, Q_{cond}, is the amount of charge transported across the phosphor layer which gives rise to light emission and is used to calculate the ACTFEL efficiency. The applied voltage waveform and a Q-F_p curve for sample a is shown in Fig. 5.8 for convenience in explaining how Q-F_p parameters are assessed and what they correspond to physically[79,80]; this is done as follows.

F_{ss} is the phosphor electric field at which steady-state or field-clamping occurs. Q_{relax} is the relaxation charge which flows through the phosphor layer when the applied voltage is at its maximum value. Q_{leak} is the leakage charge emitted from the shallow interface states during the portion of the waveform in which the applied voltage is zero. Q_{pol} is the polarization charge which

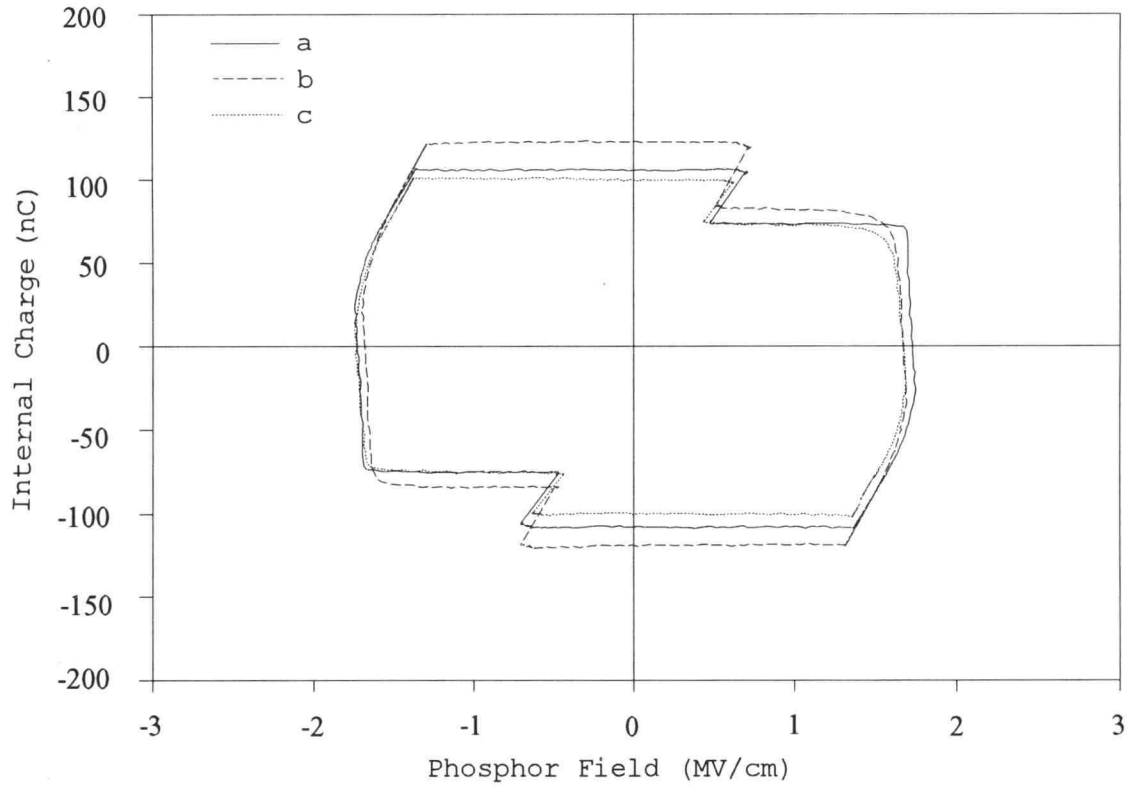

Fig. 5.7 Q-F_p characteristics of ACTFEL devices a, b, and c.

remains at the phosphor-insulator interface when the applied voltage changes its polarity. + and - superscripts correspond to a positive or negative applied voltage pulse.

Of the Q-F_p parameters collected in Table 5.2, Q_{cond} and Q_{leak} are most important parameters for assessment of the ACTFEL performance. A large value of Q_{cond} is desirable since this is the transported charge giving rise to impact excitation and, ultimately, light. Q_{cond} of sample c is smaller than that of a or b. A better ACTFEL performance

index is the ratio of leakage to conduction charge, which is also included in Table 5.2. This ratio should be as small as possible for optimal ACTFEL performance. A large leakage charge, Q_{leak}, corresponding to a reduction in the polarization field which aids the subsequent voltage pulse, is known to degrade the electrical performance of ACTFEL devices. Ultimately, electrical performance indexes such as the leakage to conduction charge ratio cannot be expected to provide a reliable measure of the ACTFEL performance. Rather, an ACTFEL device is an optoelectrical device whose performance must be evaluated from an efficiency defined in terms of an optical output and an electrical input; such an assessment is performed in the following section.

Finally, note from Table 5.2 that the electrical properties of these ACTFEL devices with SiON dielectrics are relatively symmetric (i.e. independent of the applied voltage polarity). Additionally, the steady-state phosphor field, Fss, is the same, to within experimental error, for all three of the ACTFEL devices studied.

5.2.5 Discussion

The ACTFEL device efficiency, η, is calculated as follows [84].

$$\eta = \frac{\pi L \times 10^2}{2V_{th}^{p} f \Delta Q}, \quad [\mathrm{lm/W}] \qquad (5.2)$$

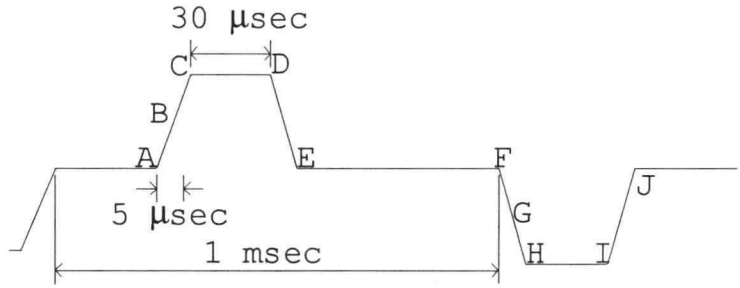

(a)

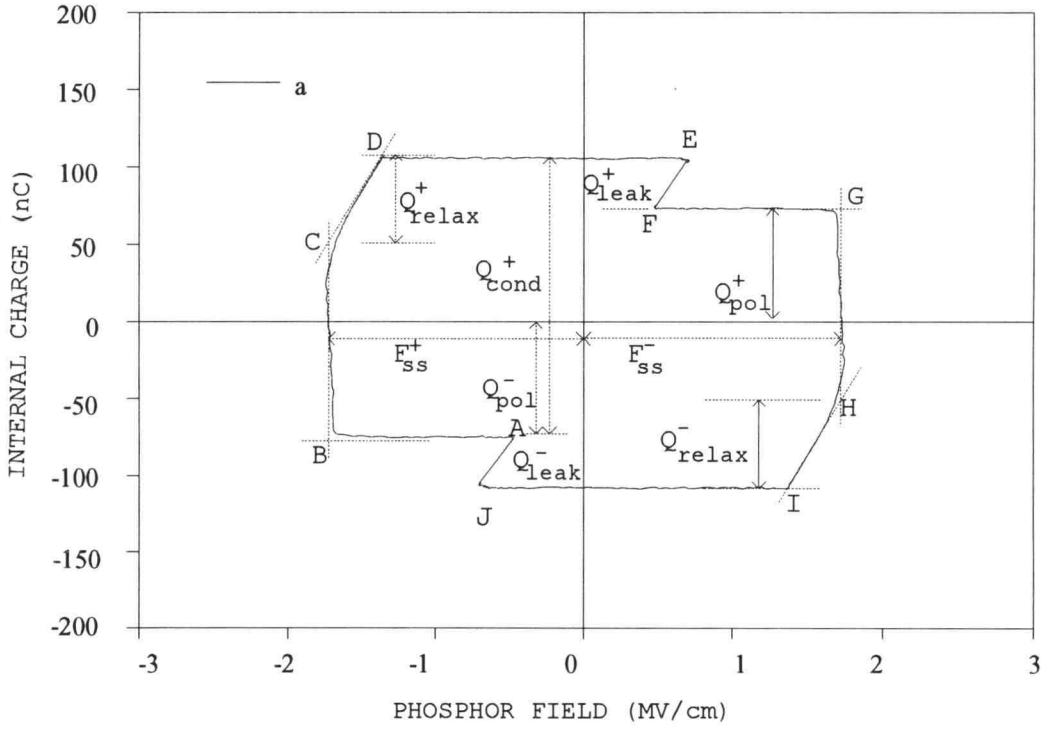

(b)

Fig. 5.8 (a) Applied voltage waveform and (b) Q-F_p curve of an ACTFEL device with labels A-J indicating a correspondence between the applied voltage waveform and the Q-F_p curve.

Table 5.2 ACTFEL parameters deduced from Q-F_p characteristics.

Measured Parameters	a		b		c	
	+	-	+	-	+	-
F_{ss} [MV/cm]	1.73	1.73	1.7	1.68	1.73	1.7
Q_{leak} [nC/cm^2]	418	418	532	468	342	291
Q_{relax} [nC/cm^2]	759	722	975	797	759	671
Q_{cond} [nC/cm^2]	2278	2278	2633	2570	2203	2152
Q_{pol} [nC/cm^2]	924	937	1051	1051	924	937
Q_{leak}/Q_{cond} [%]	18.3	18.3	20.2	18.2	15.5	13.5
Q_{leak}/Q_{cond} [%] Average per Cycle	18.3		19.2		14.5	

where L[Cd/m^2] : luminance

f[Hz] : frequency

ΔQ[μC/cm^2] : conduction charge density

V_{th}^p : threshold voltage of the phosphor layer ($V_{th}^p = \frac{C_i}{C_i + C_p} V_{th}$).

The threshold voltage, V_{th}, and the luminance, L, at V_{th} + 40V are deduced from the L-V curve shown in Fig. 5.5. The threshold voltage of the phosphor layer, V_{th}^p (i.e. internal threshold voltage), is calculated from $V_{th}^p = \frac{C_i}{C_i + C_p} V_{th}$, where C_i and C_p are measured from the C-V curves indicated

in Fig. 5.6. Finally, the conduction charge density, ΔQ, which is the same as Q_{cond}, is measured from the Q-F_p curve shown in Fig. 5.7. The parameters needed to calculate the ACTFEL efficiency are tabulated in Table 5.3.

As shown in Table 5.3, sample c has the highest efficiency and the efficiency trend is $\eta_c > \eta_b > \eta_a$. The efficiency of the sample c is improved by approximately 35.5 % compared to that of sample a, and approximately 13.5 % compared to that of sample b. Note that the

Table 5.3 ACTFEL parameters related to efficiencies.

ACTFEL Parameter	Sample a	sample b	sample c	Comments
Thickness(I) [Å]	3600	2900	3418	PECVD
Thickness(P) [Å]	6200	6200	6200	Thermal Evaporation
C_i [nF]	1.5	1.75	1.65	
C_p [nF]	1.0	1.034	0.993	C-V graph
C_t [nF]	0.6	0.65	0.62	
V_{th} [V]	179	162	164	L-V
V_{th}^p [V]	107.4	101.8	102.4	$V_{th} C_i / (C_i + C_p)$
L(V_{th}+40V) [fL]	481	635	606	L-V
η(V_{th}+40V) [lm/W]	1.062	1.268	1.439	L-V, Q-F_p

efficiency trend, $\eta_c > \eta_b > \eta_a$, is the same as that of the transmittance, $T_c > T_b > T_a$, discussed in section 5.2.1. Thus, this improvement of the ACTFEL efficiency is attributed to the optically-engineered multiple dielectric layer designed for the maximum optical transmittance.

5.3 Summary

In this chapter, an ACTFEL device with inhomogeneous SiON insulating layers is designed to have maximum optical transmittance, fabricated, and tested in an attempt to increase the ACTFEL efficiency compared to that of conventional ACTFEL structures. From L-V, C-V and Q-F_p analysis it is found that the efficiency of the ACTFEL device can be improved by optical engineering using multiple SiON insulators.

Chapter 6. Conclusions and Recommendations for Future Work

6.1 Conclusions

In this thesis, computer-controlled plasma-enhanced chemical deposition (PECVD) is employed to grow inhomogeneous silicon oxynitride (SiON) layers with refractive indices ranging from 1.46 to 2.05. Compositional control of the inhomogeneous SiON layers is achieved using a Techware PAL-68000 process automation system to control flow rates of reactant gases in real-time. Several optical coatings and devices are designed, fabricated, and tested in order to demonstrate a proof-of-concept of inhomogeneous dielectrics grown by PECVD.

The major accomplishments achieved by computer-controlled PECVD are:

1. A SiON calibration chart is constructed, in which the relationships between refractive index and deposition rate as a function of N_2O/N_2 flow rate ratio is established.

2. Linearly graded and superlattice-like SiON layers with a refractive index variation of 1.46 to 2.05 are grown on a silicon substrate. Compositional profiles for these devices are obtained by AES sputter profiling.

3. AR coatings with a continuously varying refractive index are fabricated on glass substrates. Good agreement is obtained between the simulated and measured optical reflectance spectra.

4. ACTFEL devices employing PECVD-grown SiON multilayer insulators are realized in order to demonstrate an improvement in the optical outcoupling efficiency. It is found that the efficiency of the multiple layer SiON ACTFEL device increases by approximately 14% compared to that of the conventional ACTFEL device structure.

5. Rugate filters with a sinusoidally varying index of refraction profile are grown on glass substrates. The excellent agreement obtained between simulated and measured optical reflectance characteristics demonstrates the effectiveness of computer-controlled PECVD for the growth of inhomogeneous SiON dielectric layers.

6.2 Recommendations for Future Work

The viability of growing high-quality inhomogeneous SiON films by computer-controlled PECVD is demonstrated in this thesis. There are various areas of application in which this work can be extended.

1. Planar optical waveguides:

   -PECVD grown SiON optical waveguides are considered very important for opto-electronic integrated circuits (OEIC) applications[85-89]. By employing an inhomogeneous SiON layer it may be possible to reduce the tail of the electric field distribution[90] which exists outside the planar waveguide and, hence, achieve superior optical guiding.

2. Dielectric superlattice:

   -SiO_2 and Si_3N_4 are known to have wide bandgaps of approximately 8 eV and 5 eV, respectively. Therefore, very deep potential wells may be formed by growing a SiO_2/Si_3N_4 dielectric superlattice structure. Quantization of energy may occur in the potential wells. Although such dielectric superlattices were grown as a part of this thesis research, measurements such as synchrotron absorption or cathodoluminescence are needed to verify the existence of quantum mechanical effects in the dielectric superlattice structures.

3. More advanced applications of rugate filters:

   -The sidelobes of conventional rugate filters may be eliminated by modulation of the envelope of the sinusoidally varying SiON index profile. Thus, the

performance of a rugate filter may be significantly improved if the sinusoidally varying composition profile is appropriately modulated.

4. Different material systems:
   -The SiON material system is used exclusively in the research presented herein for the realization of inhomogeneous dielectrics. Other material systems should be explored. In particular, for rugate filter applications it is desirable to have a larger dynamic range of refractive index variation (e.g. 1.46-2.3); this may be achieved using other material systems [91,92]. one promising candidate is the SiO_2-TiO_2 (SiTiO) ternary system.

5. Improvements in the control of PECVD dielectrics:
   -There is a transient response time characteristic of the PECVD system due to the capacitive nature of the chamber and the response time of the MFC. Upon receiving a control signal from the PAL-68000 controller, it takes approximately two seconds for the MFC of the PECVD system to reach a constant gas flow rate. If the transfer function of the PECVD system (specifically, the MFC) is evaluated, then it may be possible to design an input voltage waveform for the PAL-68000 to achieve more precise compositional

control.

6. Inhomogeneous dielectrics by other technologies:
-Other deposition technologies besides PECVD should be employed for the growth of inhomogeneous dielectrics. A prime candidate is electron cyclotron resonance chemical vapor deposition (ECRCVD)[93,94] since high quality SiO_2 and Si_3N_4 films have been grown at room temperature using this technology.

BIBLIOGRAPHY

[1] Z.Knittl, in *Optics in Thin Films*, (John Wiley & Sons, New York, 1976)

[2] H.M.Liddell, in *Computer-aided Techniques for the Design of Multilayer Filters*, (Adam Higler Ltd, Bristol, 1981)

[3] H.A.Macleod, in *Thin-Film Optical Filters*, (Macmillan Publishing Co., New York, 1986)

[4] A.Thelen, in *Design of Optical Interference Coatings*, (McGraw-Hill Inc., 1989)

[5] J.D.Rancourt, in *Optical Thin Films User's Handbook*, (Macmillan Publishing Company, New York, 1989)

[6] R.Jacobsson, "Matching a Multilayer to a High Refractive Index Substrate by Means of an Inhomogenous Layer," J. Opt. Soc. Am., Vol.54, pp.422-423, 1964

[7] R.Jacobsson and J.O.Martensson, "Evaporated Inhomogeneous Thin Films," App. Opt. Vol.5, No.1, pp.29-34, 1966

[8] R.Jacobsson, "LIGHT REFLECTION FROM FILMS OF CONTINUOUSLY VARYING REFRACTIVE INDEX," Prog. Opt., Vol.5, pp.246-285, 1966

[9] R.Jacobsson, in *Physics in Thin Films*, edited by G.Hass, M.Francombe and R.W.Hoffman,(Academic:New York, 1975), Vol.8, pp.51-98

[10] H.Sankur and W.H.Southwell, "Broadband gradient-index antireflection coating for ZnSe," Appl. Opt., Vol.23, No.18, pp.2770-2773, 1984

[11] A.B.Harker and J.F.Denatale, "Tailored Target Approach to the deposition of gradient index optical filters," Thin Solid Films, pp.185-192, 1988

[12] R.Bertram, M.F.Ouellette, and P.Y.Tse, "Inhomogeneous optical coatings: an experimental study of a new approach," Appl. Opt., Vol.28, No.14, pp.2935-2939, 1989

[13] M.F.Ouellette, R.V.Lang, K.L.Yan, R.W.Bertram, R.S.Owles, and D.Vincent, "Experimental studies of inhomogeneous coatings for optical applications," J. Vac. Sci. Technol.A, Vol.9, No.3, pp.1188-1192, 1991

[14] P.G.Snyder, Yi-Ming Xiong, J.A.Woollam, and G.A.Al-Jumaily, "Graded refractive index silicon oxynitride thin film characterized by spectroscopic ellipsometry," J. Vac. Sci. Technol.A, Vol.10, No.4, pp.1462-1466, 1992

[15] L.Sossi, "A Method for the Synthesis of Multilayer Interference Coatings," Eesti NSV Tead. Akad. Toim. Fuus. Mat.23, pp.229-237, 1974

[16] L.Sossi, "On the Theory of the Synthesis of Multilayer Dielectric Light Filters," Eesti NSV Tead. Akad. Toim. Fuus. Mat.23, pp.171-176, 1976

[17] J.A.Dobrowolski and D.Lowe, "Optical Thin film synthesis program based on the use of Fourier transforms," Appl. Opt. Vol. 17, No.19, pp.3039-3050, 1978

[18] E.Berkcan and G.H.Cohen, "A new CAD technique for (narrow band) inhomogeneous thin film filters," SPIE, Vol.518, pp.98-104, 1984

[19] P.Baumeister, "Simulation of a rugate filter via a stepped-index dielectric multilayer," Appl. Opt., Vol.25, No.16, pp.2644-2645, 1986

[20] J.A.Dobrowolski, "Comparison of the Fourier transform and flip-flop thin-film synthesis method," Appl. Opt. Vol.25, No.12, pp.1966-1972, 1986

[21] G.Bovin and D.St.-Germain, "Synthesis of gradient-index profiles corresponding to spectral reflectance derived by inverse Fourier transform," Appl. Opt. Vol.26, No.19, pp.4209-4213, 1987

[22] Bertrand G. Bovard, "Derivation of a matrix describing a rugate dielectric thin film," Appl. Opt. Vol.27, No.10, pp. 1998-2005, 1988

[23] Bertrand G. Board, "Rugate filter design: the modified Fourier transform technique," Appl. Opt. Vol.29, No.1, pp.24-30, 1990

[24] P.G.Verly and J.A.Dobrowolski, "Iterative correction process for optical thin film sysnthesis with the Fourier transform method," Appl. Opt., Vol.29, No.25, pp.3672-3684, 1990

[25] S.Lim, J.H.Ryu, J.F.Wager, and L.M.Casas, "Inhomogeneous dielectrics grown by plasma-enhanced chemical vapor deposition," ICMCTF,93, San Diego, CA

[26] R.B.Muchmore, "Optimum Band Width for Two Layer Anti-reflection Films," J. Opt. Soc., Am. Vol.38, No.1, pp.20-26, 1947

[27] J.T.Cox and G.Hass,"Antireflection Coatings for Germanium and Silicon in the Infrared," J. Opt. Soc. Am., Vol.48, No.10, pp.677-680, 1958

[28] L.Young, "Synthesis of Multiple Antireflecton films over a rescribed frequency Band," J. Opt. Soc. Am., Vol.51, No.9, pp.967-974, 1959

[29] L.A.Catalan, "Some Computed Optical Properties of Antireflection Coatings," J. Opt. Soc. Am., Vol.52, No.4, pp.437-440, 1961

[30] J.T.Cox ,G.Hass, and A.Thelen, "Triple-Layer Antireflection Coatings on Glass for the Visible and Near Infrared," J. Opt. Soc. Am., Vol.52, No.9, pp.965-969, 1962

[31] I.Lubezky and A.Lubezky, "Practical design of double-layer antireflective coatings for high-index substrates," Opt. Eng., Vol.22, No.6, pp.753-755, 1983

[32] W.H.Southwell, "Coating design using very thin high- and low-index layers," Appl. Opt., Vol.24, No.4, pp.457-460, 1985

[33] T.Inoguchi, M.Takeda, Y.Kakihara, and M.Yoshida, "Stable High Luminance Thin-Film Electroluminescent Panels," Digest 1974 SID Int. Sym., Los Angeles, p.84, 1974

[34] J.M.Hurd and C.N.King, Pysical and Electrical Characterization of co-deposited ZnS:Mn Electroluminescent Thin Film Structures," J. Electronic Materials. Vol.8, p.879, 1979

[35] S.Tanaka, "Color electroluminescence in alkaline-earth sulfide thin-films," J. Luminesce., Vol.40 & 41, pp.20-23, 1988

[36] E.Beringuier, "Charge transfer in ZnS-type electroluminescence," J. Appl. Phys., Vol.66, No.3, pp.1314-1325, 1989

[37] R.Mach and G.O.Mueller, "Physics and technology of thin film electroluminescent displays," Semicond. Sci. Technol., Vol.6, pp.305-323, 1991

[38] J.D.Davidson, J.F.Wager, I.Khormaei, C.N.King, and R.Williams, "Electrical characterization and modeling of alternating-current thin film electroluminescent devices," IEEE Trans. Electron Devices, Vol.39, No.5, pp.1122-1128, 1992

[39] A.Herpin, Comp. rend. Vol. 225, pp. 182, 1947

[40] F. Abelès, "Recherches sur la propagation des ondes lectromagnetiques sinusoidales dans les milieus stratifi s," Ann. Phys., Paris 12th series, Vol.5, pp.596-640 and pp.706-784, 1950

[41] O.S.Heavens, *Optical Properties of Thin Solid Films*, (Dover Publications, New York, 1965)

[42] P.H.Berning, in *Physics of Thin Films*, edited by G.Hass, M.Francombe, and R.W.Hoffman, (Academic:New York, 1963), Vol.1, pp.69-121

[43] P.Baumeister, "Design of multilayer filters by succesive approximations," J. Opt. Soc. Am., Vol.48, p.955, 1958

[44] J.A.Dobrowolski, "Completely automatic synthesis of optical thin film systems," Appl. Opt., Vol.4, pp.937-946, 1965

[45] P.P.Michiels, L.A.Verhoef, J.C.Stroom, W.C.Sinke, R.J.C.van Zolingen, C.M.M.Denisse, and M.Hendriks, "Hydrogen passivation of polycrystalline silicon solar cells by plasma deposition of silicon nitride," IEEE 21st Photovoltaic Specialist Conf., pp.638-643, 1990

[46] B.L.Sopori, "Effects of encapsulation on the performance of silicon solar cells," IEEE 21st Photovoltaic Specialist Conf., pp.618-623, 1990

[47] N.Shibata, "Improvement of Solar Cell Performance Using Plasma-Deposited Silicon Nitride Films with Variable Refractive Indices," Jap. J. Appl. Phys., Vol.27, No.4, pp.480-484, 1988

[48] Y.Katagiri and H.Ukita, "Ion beam sputtered $(SiO_2)_x(Si_3N_4)_{1-x}$ antireflection coatings on laser facets produced using O_2-N_2 discharges," Appl. Opt., Vol.29, No.34, pp.5074-5079, 1990

[49] L.I.Epstein, "The Design of Optical Filters," J.Opt.Soc.Am., Vol.42, No.11, pp.806-810, 1952

[50] M.C.Ohmer, "Design of three-layer equivalent films," J. Opt. Soc. Am., Vol.68, No.1, pp.137-139, 1978

[51] A.Thelen, "Design of Optical Minus Filters," J. Opt. Soc. Am., Vol.61, No.3, pp.365-369,1971

[52] P.Baumeister, "Theory of rejection filters with ultranarrow bandwidths," J. Opt. Soc. Am., Vol.71, No.5, pp.604-606, 1981

[53] P.W.Baumeister and J.M.Stone, "Broad-band Multilayer Film for Fabry-Perot Interferometer," J. Opt. Soc. Am., Vol.46, pp.228-229, 1956

[54] A.Thelen, "Multilayer Filters with Wide Transmittance Bands," J. Opt. Soc. Am., Vol.53, No.11, pp.1266-1270, 1963

[55] O.S.Heavens and H.M.Liddel, "Staggered Broad-Band Reflecting Multilayers," Appl. Opt., Vol.5, No.3, pp.373-376, 1966

[56] A.Thelen, "Equivalent Layers in lMultilayer Filters," J. Opt. Soc. Am., Vol.56, No.11, pp.1533-1538, 1966

[57] A.Thelen, "Multiplelayer filters with wide transmittance bands, II," J. Opt. Soc. Am., Vol.63, No.1, pp.65-68, 1973

[58] A.Thelen, "Nonpolarizing edge filters," J. Opt. Soc. Am., Vol.71, No.3, pp.309-314, 1981

[59] W.H.Southwell, "Spectral response calculations of rugate filters using coupled-wave theory," J. Opt. Soc. Am., Vol.5, No.No.9, pp.1558-1564, 1988

[60] P.Yeh, *Optical Waves in Layered Media*, (Wiley, New York, 1988)

[61] W.H.Southwell, "Using apodization functions to reduce sidelobes in rugate filters," Appl. Opt., Vol.28, No.23, pp.5091-5094, 1989

[62] S.M.Ojha, in *Physics of Thin Films*, edited by G.Hass, M.Francombe, and R.W.Hoffman, (Academic:New York, 1963), Vol.12, pp.237-296

[63] J.A.Thorton, "Plasma-Assisted Deposition Processes: Theory, Mechanisms, and Applications," Thin Solid Films, Vol.107, pp.3-19, 1983

[64] A.Sherman, "Plasma-Assisted Chemical Vapor Deposition Processes and Their Semiconductor Applications," Thin Solid Films, Vol.113, pp.135-149, 1984

[65] D.W.Hess, "Plasma-surface interactions in Plasma-Enhanced Chemical Vapor Deposition," Ann. Rev. Mater. Sci, Vol.16, pp.163-183, 1986

[66] F.Jansen, in *Plasma Deposited Thin Films*, edited by J.Mort and F.Jansen, (CRC Press, Inc.:Florida, 1986), pp.1-19

[67] M.Hirose, in *Plasma Deposited Thin Films*, edited by J.Mort and F.Jansen, (CRC Press, Inc.:Florida, 1986)

[68] W.D.Partlow, "Plasma CVD: new ways to control thin film deposition processes," SPIE, Vol.678, pp.24-30, 1986

[69] B.Chapman, in *Glow Discharge Process*, (Wiley, New York, 1980)

[70] PAL-68000 Programmer's Manual, Techware Systems Corporation, 1989

[71] Instruction Manual for MKS 2259B Mass Flow Meter and Flow Controller, MKS Instruments, Inc.

[72] D.K.Schroder, in *Semiconductor Material and Device Characterization*, (Wiley, New York, 1990)

[73] D.E.Aspense and A.A.Stunda, "High Precision Scanning Ellipsometer," Appl. Opt., Vol.14, No.1, pp.220-228, 1975

[74] D.Briggs and M.P.Seah(Ed.), in *Practical Surface Analysis*, (Wiley, Chichester, 1983)

[75] R.E.Honig, "Surface and Thin Film Analysis of Semiconductor Materials," *Physics of Thin Films*, Vol. 31, edited by G.Hass, (New York: Academic), pp.89-122, 1976

[76] J.D.Davidson, Oregon State University, MS Thesis, 1991

[77] R.C.McArthur, J.D.Davidson, J.F.Wager, I.Khormaei, and C.N.King, "Capacitance-voltage characteristic of alternating-current thin-film electroluminescent devices," Appl. Phys. Lett., Vol.56, No.19, pp.1889-1891, 1990

[78] J.F.Wager, A.A.Douglas, and D.C.Morton, "Electrical Characterization and Modeling of ACTFEL Devices," Electroluminescence, edited by V.P.Singh and J.C.McClure, (El Paso, TX, Cinco Puntos Press, 1992), p.92

[79] A.Abu-Dayah, S.Kobayashi, and J.F.Wager, "Internal Charge-Phosphor Field Characteristics of Alternating-current Thin-film Electroluminescent Devices," Appl. Phys. Lett., accepted for publication.

[80] A.Abu-Dayah, J.F.Wager, and S.Kobayashi, Electrical Characterization of Atomic Layer Epitaxy ZnS:Mn Alternating-current Thin-film Electroluminescent Devices Subject to Various Waveforms," J. Appl. Phys., accepted for publication.

[81] Wie Ming Ang, Oregon State University, MS Thesis, 1993

[82] R.E.Collin, in *Foundations for microwave engineering*, (McGraw-Hill, New York, 1966)

[83] Touchstone and Libra Reference Version 2.1, EEsof, Inc., 1990

[84] Y.A.Ono, H.Kawakami, M.Fuyama, and K.Onisawa, "Transferred Charge in the Active Layer and EL Device Characteristics of TFEL Cells," Jap. J. Appl. Sci., Vol.26, No.9, pp.1482-1492, 1987

[85] D.E.Zelmon, H.E.Jackson, J.T.Boyd, A.Naumaan, and D.B.Anderson, "A low-scattering graded-index SiO_2 planar optical waveguide thermally grown on silicon," Appl. Phys. Lett., Vol.42, No.7, pp.565-566, 1983

[86] I.K.Naik, "Low-loss integrated optical waveguides fabricated by nitrogen ion implantation," Appl. Phys. Lett., Vol.43, No.6, pp.519-520, 1983

[87] R.A.Soref and J.P.Lorenzo, "Silicon Guided-Wave Optics," Solid State Technol., pp.95-98, Nov., 1988

[88] A.Aboudou, E.Goutain, J.P.Vilcot, M.Fracois, L.Joannes, and D.Decoster, "Monolithic integration of GaAs MSM photodetector and SiO_2/Si_3N_4 dielectric optical waveguide," Electron. Lett., Vol.28, No.1, pp.52-53, 1992

[89] G.Barbarossa and P.J.R.Laybourn, "Vertically integrated high-silica channel waveguides on Si," Electron. Lett., Vol.28, No.5, pp.437-438, 1992

[90] A.B.Buckman, *Guided-Wave Photonics*, (Saunders College Publishing, Fort Worth, 1992)

[91] L.M.Williams and D.W.Hess, "Structural properties of titanium dioxide films deposited in an rf glow discharge," J. Vac. Sci. Technol. A, Vol.4, No.4, pp.1810-1819, 1983

[92] D.W.Hess, "Plasma-enhanced CVD:Oxides, nitrides, transtion metals, and transition metal silicides," J. Vac. Sci. Technol. A, Vol.2, No.2, pp.244-252, 1984

[93] M.Kitagawa, T.Hirao, T.Ohmura, and T.Izumi, "Structural Properties of Silicon Oxide Films Prepared by the RF Substrate Biased ECR Plasma CVD Method," Jap. J. Appl. Phys., Vol.28, No.6, pp.1048-1050, 1989

[94] Y.Manabe and T.Mitsuyu, "Silicon nitride thin films prepared by the electron cyclotron resonance plasma chemical vapor deposition method," J. Appl. Phys., Vol.66, No.6, pp.2475-2480, 1989

[95] J.H.Ryu, private communications.